

Dielectrophoretic Characterization and Separation of Microbials on a Microfluidic Device
Based on Their Inherent Electrophysiology

A Dissertation

Presented to
the faculty of the School of Engineering and Applied Science
University of Virginia

in partial fulfillment
of the requirements for the degree

Doctor of Philosophy

by

Yi-Hsuan Su

August

2015

APPROVAL SHEET

The dissertation
is submitted in partial fulfillment of the requirements
for the degree of
Doctor of Philosophy



AUTHOR

The dissertation has been read and approved by the examining committee:

Nathan Swami

Advisor

Michael Reed

Circle Warren

James Landers

Roseanne Ford

Accepted for the School of Engineering and Applied Science:



Dean, School of Engineering and Applied Science

August
2015

Print Form

Abstract

Infectious diseases are among the leading causes of mortality across the world, after cardiovascular disease. Global health is constantly under threat due to unpredictable outbreaks of pathogenic infections. Although antibiotics are commonly used to deactivate the microorganisms, the development of resistant and persistent strains has challenged public health and highlights the need for novel diagnostic platforms that are not based on microbial culture.

Conventional analytical methods such as, polymerase chain reaction (PCR) based DNA amplification and enzyme linked immunoassay (ELISA) are labor intensive, not non-destructive and time consuming due to their need for chemical modifications. There is hence, the need for alternate point-of-care diagnostic methods that can directly analyze intact microbial cells, in a rapid and label-free manner; for the downstream development of rapid detection methods.

Microfluidic lab-on-a-chip devices provide many unique features towards point-of-care diagnostics, such as, high sensitivity and fast detection kinetics due to their large surface to volume ratios, high accuracy due to their ability for highly parallel analysis, and they require only small quantities of reagents. Characterization and separation of biological particles based on their inherent electrophysiology, to indicate characteristic phenotypes, is an emerging strategy. To address this need, we herein study microfluidic device platforms for dielectrophoretic (DEP) separation and characterization of intact microbials, by benchmarking their efficacy versus the conventional state-of-the-art in microbiological analysis.

The World Health Organization (WHO) has reported 1.7 billion cases of diarrhoeal diseases and 1.5 million fatalities every year globally. Herein, we demonstrate the application of quantitative dielectrophoretic tracking over a wide frequency range (10 kHz–10 MHz) to separate and characterize the persistent oocyst subpopulations of *Cryptosporidium parvum*, a water-borne pathogen capable of causing enteric infections^{*1*}. We also show that DEP technique can independently monitor and separate particular *C.difficile* strains, one of the most serious causes of antibiotic-associated diarrhea, based on their characteristic S-layers, which cause alterations in their electrophysiology^{*2*}. We also demonstrate these capabilities of DEP towards characterizing of the electrophysiological alterations on toxigenic *C.difficile* (TCD) strains due to the antimicrobial and anti-adhesive effects of the thermolabile extracellular factors secreted by non-toxigenic *C.difficile*, as a probiotic, during co-culture^{*9*}. We envision this non-destructive, label-free, and sensitive DEP method can be used for diagnostics and biomedical research application.

#: See List of Publications for details.

Acknowledgements

First and foremost, I would like to give my sincerest gratitude to my adviser, Dr. Nathan Swami. To Nathan: First, thank you for taking the risk accepting me, whose background is Biomedical science, as your student in the electrical engineering. Thank you for your mentorship throughout these years. I greatly appreciate your guidance and patience whenever I needed a discussion, some advice or just a comment. Your advice and training have been priceless to me! This dissertation would not have been possible without you. Thank you very much! I would also like to thank my group mates for the friendship, discussion and helping me for the qualifying exam: Ali Rohani, Walter Varhue and Mikiyas Tsegaye. Special thanks to Ali for all the fun time doing experiments together and explaining to me the “beautiful” equations. Special thanks to Walter for being so patient explaining to me the circuit model so many times. Special thanks to Mikiyas for helping me with the courses and many conceptual questions.

I would like to express my appreciation to our collaborators at the center of Infectious Diseases in the School of Medicine. Special thanks to Dr. Cirle Warren for providing me the direction in my research from the clinical point of view, and thank you for including me to the C.diff group to learn other people’s research. I would also like to thank Dr. Richard Guerrant for his guidance in my research and everyone in Dr. Guerrant’s lab for their help when I needed: John Moore, Glynis Kolling, David Bolick and Edna Zaenker.

I would also like to thank the staff in the ECE department front office: Yadi Weaver, Dan Fetko, Susan Malone and Gloria Walker. Thank you all for the friendship, support, kindness, advice and help when I needed it.

I am grateful to have many friends supporting me through this journey: Thank you Ashley Chaplin for adding spice to my life in Charlottesville. Thank you Darya Levashova, Toni Kember, Brian Twitty, Shana Craft and Kamram Munira for the fun time together in Charlottesville. Thank you Der-You Kao for many stress-relieving chats and offering me a place for my weekend getaways. Thank you my old friends in Taiwan for always being there for me: Li-Fu Lin, Lei-Ling Chen, Wei-Ju Liao and Yung-Ru Lo. I would also like to thank Uncle Yung-Chung Kao and Aunt Cherry Kao for their kind hospitality and advice for my acclimation into US life.

Finally, I would like to express my deepest gratitude to my family: my parents, Jui-Yuan Su and Pi-Chen Kao, my aunt Jui-Ching Su, my cousin Ching-Ying Lin and my sister Hsin-I Su, words cannot express how appreciative I am of their loving support. Their constant love, concern and support have helped me through all these years. I would not be here without them.

Dedication

For Mark Kao,
who gave me strength and courage everyday through these difficult years.

Table of Contents

Abstract	i
Acknowledgements	ii
Table of Contents	iv
List of Publications (* directly related to this thesis)	vii
Chapter 1 <i>Introduction</i>	1
<i>Dielectrophoresis</i>	3
<i>Shell Model for biological particles</i>	6
<i>Electrorotation</i>	7
<i>Cryptosporidium parvum</i>	9
<i>Clostridium difficile</i>	10
Chapter 2 <i>Methodology</i>	12
<i>Electrode-less Dielectrophoretic experimental setup</i>	12
<i>Computing dielectrophoretic spectra from particle velocity measurements</i>	13
<i>Image analysis on Electrode-based DepTech 3DEP reader</i>	14
Chapter 3 <i>Dielectrophoretic characterization and separation of Cryptosporidium parvum</i>	17
I. Quantitative Dielectrophoretic tracking for characterization and separation of persistent <i>Cryptosporidium parvum</i>	17
<i>Introduction and Rationale</i>	17
<i>Objectives</i>	19
<i>Materials and methods</i>	19
Preparation of <i>Cryptosporidium parvum</i> oocysts	19
Disinfection treatments on oocysts	20
Fluorescence monitoring of oocysts	20
Excystation of oocysts and mouse model infectivity studies	21
<i>Results and Discussions</i>	22

Identifying persistent subpopulations after disinfection	22
Heterogeneous modification of oocysts after disinfection	23
Frequency-selective dielectrophoretic spectra	25
Separation based on oocyst wall and sporozoite infectivity	28
II. Dielectrophoretic characterization of silver nanoparticle induced disinfection action on oocysts of <i>Cryptosporidium parvum</i> : Effect of nanoparticle functionalization	30
<i>Introduction and Rationale</i>	30
<i>Results and Discussions</i>	31
Effect of AgNPs capping layer on their morphological modifications to oocysts	31
Effect of AgNPs capping layer on their modifications to the excystation behavior of oocysts	33
Frequency-selective dielectrophoretic spectra of each AgNP capping layer	35
Effect of AgNPs capping layer on their disinfection action on mice model	36
III. Conclusions	37
Chapter 4 Dielectrophoretic characterization and separation of <i>Clostridium difficile</i>	40
I. Independent dielectrophoretic monitoring and separation of individual <i>Clostridium difficile</i> strains based on their S-layer proteins	40
<i>Introduction and Rationale</i>	40
<i>Objectives</i>	41
<i>Material and Methods</i>	42
<i>C.difficile</i> sample preparation	42
Adhesion assay	43
Growth measurement	43
Toxicity enzyme-linked immunosorbent assay	44
Sample preparation for transmission electron microscope imaging	44
Dielectrophoretic characterization of <i>C.difficile</i>	45
<i>Results and Discussions</i>	46
Morphological differences between <i>C.difficile</i> strains	46
Independent dielectrophoretic monitoring of each <i>C.difficile</i> strain	49

Alterations to each <i>C.difficile</i> strain upon vancomycin treatment	52
Benchmarking DEP velocities to toxin production and growth rate	54
Inter-strain separations from mixed <i>C.difficile</i> samples	57
II. Single cell level analysis of the inhibitory effect of non-toxigenic <i>C.difficile</i> on toxigenic <i>C.difficile</i>	58
<i>Introduction and Rational</i>	58
<i>Objectives</i>	60
<i>Results and Discussions</i>	61
Inhibition of HTCD cell functionalities in NTCD supernatant and co-cultured with NTCD	61
Dielectrophoretic monitoring of HTCD modification	63
III. Conclusions	66
Chapter 5 <i>Conclusion and Future work</i>	68
<i>Conclusion</i>	68
<i>Future work</i>	70
DEP separation of <i>C.difficile</i> from other microbials in fecal samples	70
DEP separation of <i>C.difficile</i> from probiotics after mixed culture	71
Bibliography	73

List of Publications (* directly related to this thesis)

- *1*. **YH Su**, M Tsegaye, W Varhue, KT Liao, L Abebe, J Smith, RL Guerrant and NS Swami. "Quantitative dielectrophoretic tracking for characterization and separation of persistent subpopulations of *Cryptosporidium parvum*" *Analyst* (2014) 139, 66-73 (Selected as "Hot article" and Cover page) (Impact Factor, IF=4.2)
- *2*. **YH Su**, C Warren, RL Guerrant, NS Swami. "Dielectrophoretic monitoring and inter-strain separation of intact *Clostridium difficile* based on their S(surface)-layers" *Analytical Chemistry* (2014) 86, 10885-63 (IF=5.8)
3. V Farmehini, A Rohani, **YH Su**, NS Swami. "A wide-bandwidth power amplifier for frequency-selective insulator-based dielectrophoresis." *Lab on a Chip* (2014) 4138-4187 (IF=5.7)
4. A Rohani, W Varhue, **YH Su**, NS Swami. "Electrical tweezer for highly parallelized electro-rotation measurements over a wide frequency bandwidth" *Electrophoresis* (2014) 35, 1795-1802 (IF=3.2)
5. A Rohani, W Varhue, **YH Su**, NS Swami. "Quantifying spatio-temporal dynamics of biomarker pre-concentration and deletion in microfluidic systems by intensity threshold" *Biomicrofluidics* (2014) 8, 052009 (IF=3.7)
6. V Chaurey, A Rohani, **YH Su**, KT Liao, CF Chou, NS Swami. "Scaling down constriction-based electrodeless dielectrophoresis devices for trapping nanoscale bio-particles in physiological media of high-conductivity" *Electrophoresis* (2013) 34, 1097-1104 (IF=3.2)
7. V Chaurey, F Block, **YH Su**, PC Chiang, E Botchwey, CF Chou, NS Swami. "Nanofiber size-dependent sensitivity of fibroblast directionality to the method of alignment of the scaffold" *Acta Biomater.* (2012) 8, 3982-90 (IF=5.7)
8. **YH Su**⁺, PC Chiang⁺, LJ Cheng, CH Lee, NS Swami, CF Chou. "Controlling retraction fibres during fibroblast cell division via aspect ratio modulation of nanoimprinted PLGA grooves" (Under review)
- *9*. **YH Su**, A Rohani, W Varhue, C Warren, NS Swami. "The inhibitory effect of Non-toxicogenic *C. difficile* on toxigenic *C. difficile* single cells" (Submitted)

Chapter 1

Introduction

Infectious diseases caused by pathogenic microorganisms, such as bacteria, viruses, parasites and fungi, are one of the leading causes of mortality around the world. These diseases can be spread directly or indirectly from one person to another. These problems are particularly serious in developing countries due to lack of hygiene, limited access to purified water and limitations of diagnostic and therapeutic methods. Despite the remarkable advances in medical systems in developed countries, they too experience periodic infectious disease outbreaks within medical and livestock settings. The challenges to arresting these diseases: (1) emergence of new infectious disease strains; (2) re-emergence of old infectious diseases as antibiotic resistant strains; and (3) persistence of intractable infectious diseases^{3,4}. There are few tools current available for precise and rapid diagnosis, especially for the persistent microbial strains. Current diagnostic methods include animal model, cell cytotoxicity models, polymerase chain reaction (PCR) and Enzyme-linked immunoassay (ELISA), all of which are time consuming (takes from hours to days), labor intense, destructive, not suitable for point-of-care application and not suitable for monitoring sub-populations⁵. Hence, there is a need for an alternative rapid diagnostic method, with potential for detecting persistence in a wide range of operating environments.

Microfluidic devices enable the precise manipulation of particles in microliter scale fluidic volumes, due to the geometric constrains (1-100 μm features) that a balance of localized electrical, magnetic and viscous force fields versus inertial flows. Microfluidics offers several advantages over the conventional platforms, such as high sensitivity for separation and detection due to their high surface to volume, small sample volume requirement, fast analysis, and small device footprint⁶. These advantages have made microfluidics a potential tool to

improve and have an impact on diagnostics and biomedical research. Herein, in this work, we aim to utilize a microfluidic device based on dielectrophoresis (DEP) technique to characterize and separate microbials. Two microbials are studied: (1) *Cryptosporidium parvum* (*C. parvum*), a common waterborne parasite that causes deadly diarrheal infections in developing countries. We apply quantified DEP tracking over the frequency range of 1kHz-10MHz on characterization and separation the persistent subpopulation after disinfectant treatment. Furthermore, we utilize DEP to examine the disinfectant effect of silver nanoparticles capping layer of varying functionalization on *C. parvum* oocysts, and correlate the alterations on the oocysts to a mouse infectivity model, in vitro excystation study and morphological examination; (2) *Clostridium difficile*, a common bacteria that leads to a rapidly spreading epidemic within health-care facilities in developed countries. Herein, we utilize DEP to characterize and separate different *C. difficile* strains, which have systematic differences in their cell wall morphology due to their constituting S-layers. As a result, this difference can induce the differences in their electrophysiology due to the alterations in their cell wall capacitance. In this manner, S-layer alterations which alter the colonization ability of *C.difficile*, as benchmarked using an adhesion assay over 24 hours, can be characterized by DEP within just a few minutes. Additionally, the sensitivity of this electrophysiological method for utilizing the differences in cytoplasm conductivity to probe vancomycin-induced alterations to toxigenic *C.difficile* (TCD) and non-toxigenic *C.difficile* (NTCD) strains is benchmarked against the immunoassay and microbial growth rate methods. Furthermore, we continue to apply these DEP capabilities towards demonstration of antimicrobial and anti-adhesive effects of the thermolabile extracellular factors secreted by NTCD during co-culture, and correlate these phenotypic changes to the alterations in growth rate, toxin production and adhesion of high toxigenic *C.difficile* (HTCD). Based on the results, we envision DEP techniques can be applied towards diagnostics, biology and biomedical research in a live single-cells resolution, non-destructive and label-free manner.

Dielectrophoresis

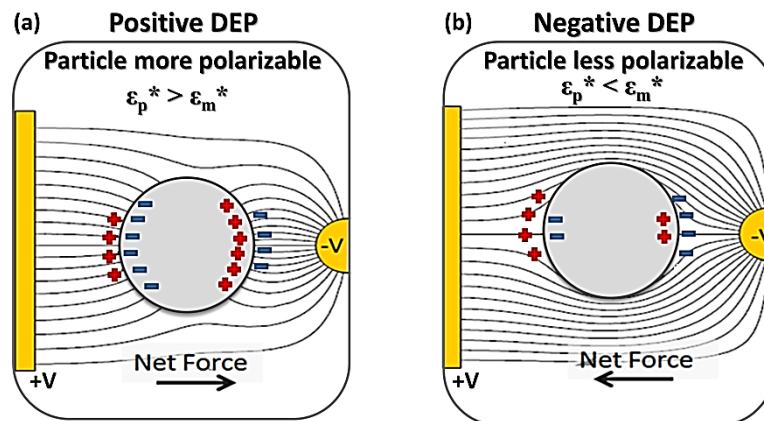


Figure 1.1: Illustration of electric field lines for the particles more polarizable (a) or less polarizable (b) than the suspending medium, in a non-uniform electric field

Dielectrophoresis (DEP) is the translation of a polarized particle under a spatially non-uniform electric field within the suspended medium. The motion does not require the particles to be charged. Upon polarization of particles within the suspending media, the spatial non-uniformity of the field drives the particles towards high field regions, as in **Figure 1.1a** (i.e. positive DEP, due to particle being more polarizable than media) or away from high field regions, as in **Figure 1.1b** (i.e. negative DEP, due to particle being less polarizable than media) towards to the high field regions within the device⁷. As per the schematic in **Figure 1.1a**, if the particle is more polarizable than the medium, then dipoles are formed to a greater extent in the particle versus the medium, thereby resulting in a net dipole moment parallel to the external field. This causes the bending of the electric field lines normal to the particle, as if it were a metal sphere; thereby translating the particle towards localized regions of high electric field strength. Conversely, if the particle has lower polarizability than the medium, then the greater charge accumulation in the medium causes the particle dipole moment to be anti-parallel to the external field. This causes screening of the electric field lines around the particle as if it were an insulator; thereby translating the particle away from the high electric field region as shown in **Figure. 1.1b**.

The polarizability of the particle is dependent on its inherent dielectric properties; i.e. permittivity (ϵ) and conductivity (σ), which exhibit a characteristic frequency response versus that of the medium (subscript: m and p for medium and particle, respectively), as given by the Clausius-Mossotti factor

$$(K_{CM}) = \left(\frac{\epsilon_p^* - \epsilon_m^*}{\epsilon_p^* + 2\epsilon_m^*} \right), \text{ where } \epsilon^* = \epsilon + (\sigma/j\omega) \dots \quad \mathbf{Eq (1)}$$

Here, ω is the angular frequency of the applied electric field. Hence, the direction of particle translation depends on the frequency response of the conductivity and permittivity of the particle. At low frequencies (< 1 MHz), the polarizability depends mainly on the conductive properties of the particles and medium, whereas at high frequencies (> 10 MHz) the respective permittivity values dominate. The trapping force (F_{DEP}) for spherical particles of hydrodynamic radius (a) is given by:

$$\mathbf{F}_{DEP} = 2\pi a^3 \epsilon_m \operatorname{Re} \left(\frac{\epsilon_p^* - \epsilon_m^*}{\epsilon_p^* + 2\epsilon_m^*} \right) \nabla E^2 = 2\pi a^3 \epsilon_m \operatorname{Re}[K_{CM}(\omega)] \nabla E^2 \quad \dots \mathbf{Eq (2)}$$

The direction of the DEP force is determined by the frequency dependent particle polarizability, i.e. the K_{CM} factor. If the $K_{CM} > 0$, the particle is trapped within the region of the strong electric field and such a motion is a PDEP response. Alternatively if the $K_{CM} < 0$, the particle is repelled from the region of the strong electric field and exhibits an NDEP response. The intensity of the DEP force depends on: (a) electric field distribution (∇E^2), (b) shape and size ($2a$) of particle; and (c) the frequency of applied voltage (ω).

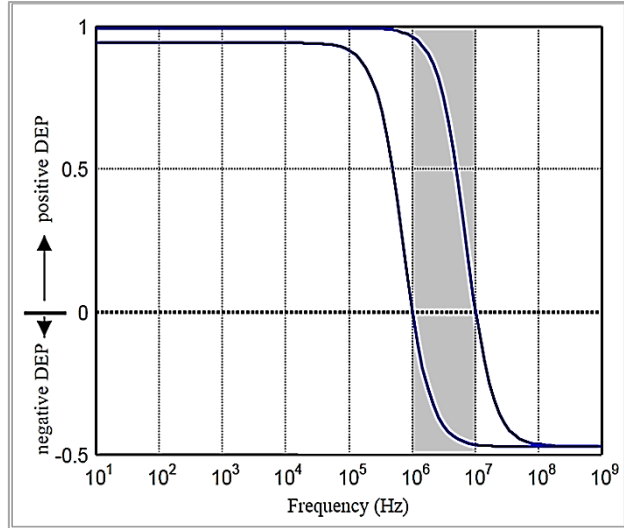


Figure 1.2: DEP force response of two homogenous particles with different conductivities (From Ref. [7])

In particles with uniform dielectric properties, we can examine the DEP force across a wide frequency spectrum by simply considering the conductivity (at low frequency) and the permittivity (at high frequency) of the particles compared to those in the medium. Based on different DEP response, we would be able to separate two different particles at particular frequency, by comparing the differences in their dielectric dispersion. For instance, the DEP responses of two homogenous particles with different conductivities are shown in **Figure 1.2**. At low frequencies ($< 1\text{MHz}$), the DEP force is constant but at different magnitude between the two particles due to their conductivity differences. In this example, the conductivities of the two particles are both higher than the medium ($K_{CM}>0$, Eq(2)), thus they experience positive DEP. At high frequencies ($> 10\text{MHz}$), the force is again constant but in the opposite sign due to the permittivity of the medium is higher than the particles ($K_{CM}<0$, Eq(2)). At mid frequencies, there is a transition of the DEP force from positive to negative, since the free charges do not have enough time to respond the field. At one particular frequency, the polarizability of the particle is the same as the medium ($K_{CM}=0$, Eq(2)), where there is zero DEP force.

Some of the distinguishing features of DEP include⁸: (a) its highly sensitive, label-free and non-destructive characterization methodology that is dependent only on the inherent dielectric properties of single bio-particles; (b) its ability to probe different dielectric regions of the bio-particle, such as its non-conducting shell versus its conducting core, based on appropriate choice of frequency of the field; and: (c) its ability to separate and enrich particular bio-particles of interest versus others in the media, due to its frequency-selectivity.

Shell Model for biological particles

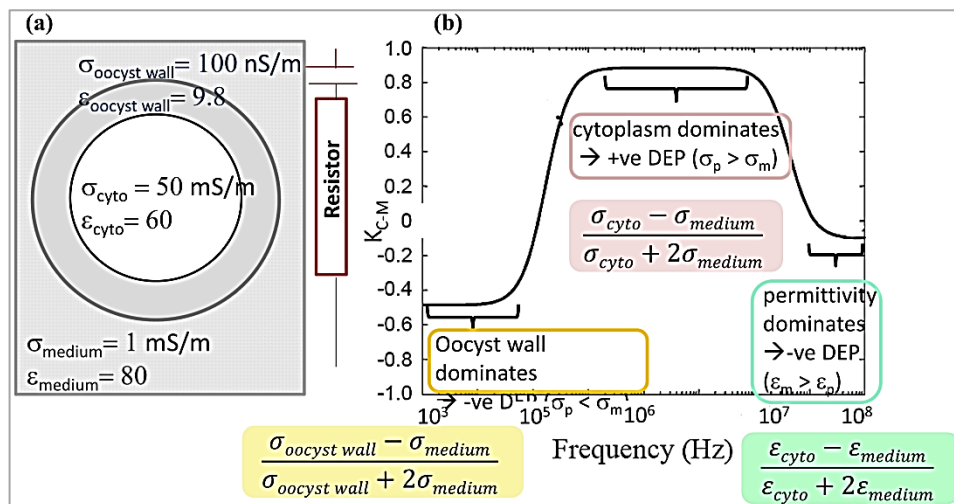


Figure 1.3: (a) Electrical model of a low conductivity oocyst wall ($\sigma_{oocyst\ wall} \sim 100 \text{ nS/m}$), which behaves as a capacitor and a high-conductivity cytoplasm ($\sigma_{cyto} \sim 50 \text{ mS/m}$) for a functional oocyst, in a medium of moderate conductivity ($\sigma_{medium} \sim 1 \text{ mS/m}$). (b) The curve shows the calculated frequency response of the cell polarizability (K_{CM}), as per Eq. (1). (Figure modified from ref. [7])

Composite biological particles, such as *Cryptosporidium parvum* oocysts or *Clostridium difficile* (more details of *C. parvum* and *C. difficile* are provided in the following sections), have a low conductivity cell membrane or oocyst wall as a shell that separates it from the conductive cytoplasm, each with relatively complicated internal structures. Hence a shell model may be used to explain the DEP response in the biological particles⁷.

Figure 1.3a shows a schematic of viable *C. parvum* with an oocyst wall (modeled as a

capacitor: C) of lower conductivity and permittivity versus that of the cytoplasm (modeled as a resistor: R). For the series RC circuit, the oocyst wall dominates at frequencies below the RC time constant, whereas the oocyst cytoplasm dominates at higher frequencies. Hence, as per the frequency response in **Figure 1.3b**, at low frequencies ($<10\text{kHz}$), negative DEP behavior occurs since: $\sigma_{\text{oocyst wall}} < \sigma_{\text{medium}}$. After a critical frequency ($\sim 400\text{kHz}$ for *C. parvum* oocysts) the oocyst cytoplasm dominates the frequency response, thereby causing positive DEP due to $\sigma_{\text{cyto}} > \sigma_{\text{medium}}$. At high frequencies ($\sim 10\text{MHz}$), we consider the permittivity rather than conductivity, hence the particles show negative DEP due to $\epsilon_{\text{cyto}} < \epsilon_{\text{medium}}$.

Electrorotation

Electrorotation (ROT) is the rotation of a polarized particle due to an electric field with a spatially dependent phase⁷. When a polarized particle is in a uniform electrical field, the induced dipole moment takes a finite amount of time to align with the vector of electric field, and become aligned with the field. If the electric field changes direction, the dipole moment must re-align itself with the changed vector of the electric field, thereby causing particle rotation. This method utilizes an external 90 degree phase shift electric field to induce dipoles on the target bio-particle that is suspended in an electrolytic medium as shown in **Figure 1.4**⁷.⁹ If the particle is more polarizable than the medium, the particle rotates along the direction of the rotating field (co-field). Conversely, if the particle is less polarizable than the medium, the particle rotates the opposite direction of the field (counter-field). The torque on the particles is given by the cross product of the field and its dipole moment¹⁰:

$$\Gamma_{ROT} = \frac{1}{2} Re[p \times E^*] = 4\pi a^3 Re[\underline{K}^1(E \times E^*)] = -4\pi\epsilon_m a^3 Im\left(\frac{\epsilon_p^* - \epsilon_m^*}{\epsilon_p^* + 2\epsilon_m^*}\right) |E|^2 \quad \dots \mathbf{Eq(3)}$$

As the equation suggests, electro-rotation depends on the imaginary part of the Clausius-Mossotti factor and the square of the electric field, with the direction of particle

rotation determined by the angle between the lagging dipole moment and the electric field.¹¹ This angle will be highly dependent on the frequency of the applied field. Besides DEP spectra, the frequency dependence of the electro-rotational spectra of a particle can also be applied to characterize the dielectric properties of different parts of composite particles. ROT methods have the ability to better discern the frequency values at which the polarization dispersion shows significant inflections, which show up as maximum or minimum values on the rotational spectrum. Herein, we utilize ROT to further confirm the observed inflections within the DEP spectra of modified microbials.

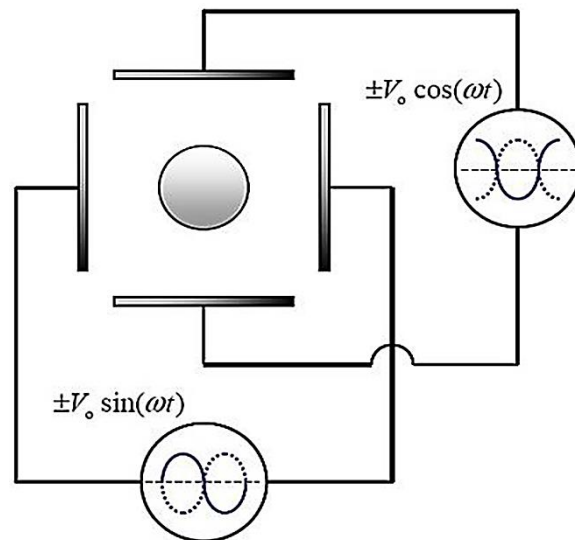


Figure 1.4: A schematic diagram of an electrorotation setup. Four signals, successively 90 degree out of phase are applied to four electrodes encircling the particle. (Figure modified from ref. [7])

Cryptosporidium parvum

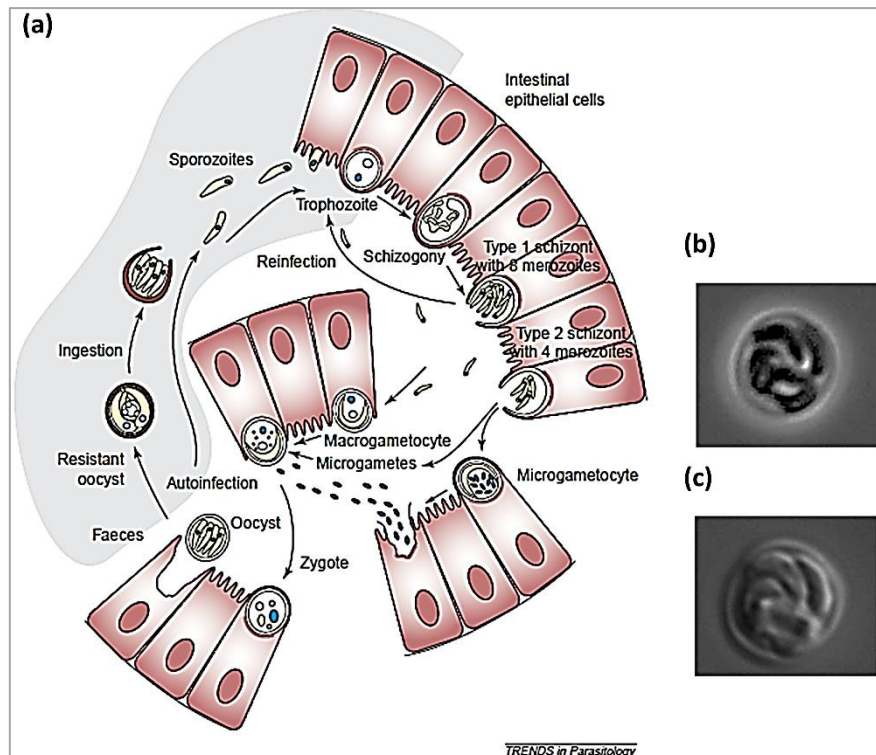


Figure 1.5: (a) Illustration of *C. parvum* life cycle (From Ref. [13]); Images of thick-walled oocyst with four sporozoites inside under (b) phase contrast or (c) differential interference contrast microscope.

Cryptosporidium is an oocyst forming protozoan parasite species of human and other vertebrates. To date, more than 20 different species have been discovered. *Cryptosporidium parvum* (*C. parvum*) is the primary species that infects the gastrointestinal tract of humans and cattle, thereby causing the gastrointestinal disease of Cryptosporidiosis, which leads to severe diarrhea. The common transmissions are from the fecal-oral route, or the ingestion of contaminated food or water. The ingestion of even low numbers of *C. parvum* oocysts (~10-100) is sufficient to cause symptomatic infection of the human gastrointestinal system and lead to fatalities within immune-compromised persons. *C. parvum* can form a thick-walled oocyst, which survives outside of its host for several months¹². Once the oocyst is ingested by a host, the banana-shaped sporozoites are released from the oocyst following exposure to body temperature, acid, trypsin and bile salts, by a process known as excystation,

and thereby start a new life-cycle in the gastrointestinal tract of the host¹³. Due to the sturdy nature of the oocyst wall, *C. parvum* oocysts are not deactivated by the standard chlorine based disinfection treatments. Cryptosporidiosis is estimated to be responsible for about 50% of the waterborne diseases attributed to parasites worldwide.

Clostridium difficile

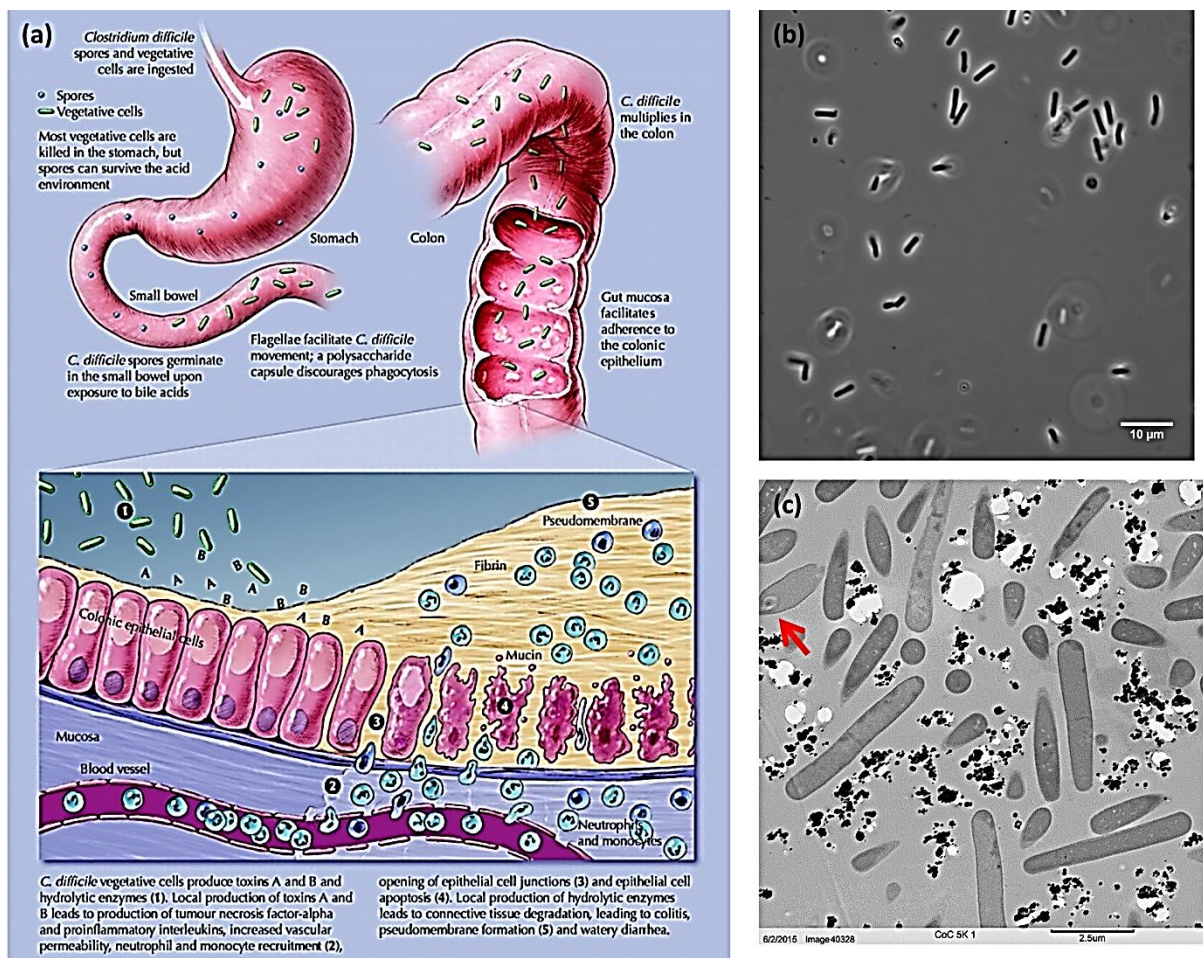


Figure 1.6: (a) Illustration of pathogenesis of CDI (adopt from ref. [14]); (b) Phase contrast image and (c) Transmission Electron Microscope image of *C. difficile*. Red arrow indicates an endospore.

Clostridium difficile (*C. difficile*) is a spore forming gram-positive anaerobic bacillus bacterium (**Figure 1.6**), which is known for causing antibiotic associate diarrhea. Healthy adults with established gut bacterial flora are resistant to *C. difficile* colonization. However, if the normal flora is altered by administration of wide-spectrum antibiotics, the risk of *C.*

difficile infection after exposure to the pathogenic organism dramatically increases¹⁴. *C. difficile* infection (CDI) is caused by the strains that produce at least one of two toxins, A and B. These strains are termed toxigenic *C.difficile* (TCD). Soon after the discovery of TCD strains, the strains of *C. difficile* that lacked toxin production were isolated from patients and were termed “non-toxigenic” *C. difficile* (NTCD). In contrast to TCD strains, NTCD strain isolates do not produce toxin A or toxin B due to the lack of Pathogenicity Locus (PaLoc), and are not typically implicated in symptomatic infection.

The spore-forming nature of *C. difficile* leads to a rapidly spreading epidemic within health-care facilities. The vegetative cells are killed in the acidic stomach environment, but spores can survive (**Figure 1.6c, red arrow**). *C. difficile* spores then germinate after exposure to bile acids, and the vegetative cells proliferate in the colon. The toxigenic strains release toxin A or/and B, and cause colitis pseudomembrane formation, which leads to diarrhea¹⁵. The usage of broad-spectrum antibiotics, hospitalization, elder and co-morbidities increase the risk of developing CDI¹⁶ and the CDI rates have exhibited a steady rise worldwide over the last two decades, with over 250,000 infections per year nationwide and 14,000 related fatalities per year, accounting for ~\$3 billion per year in health care costs.

Chapter 2

Methodology

Electrode-less Dielectrophoretic experimental setup

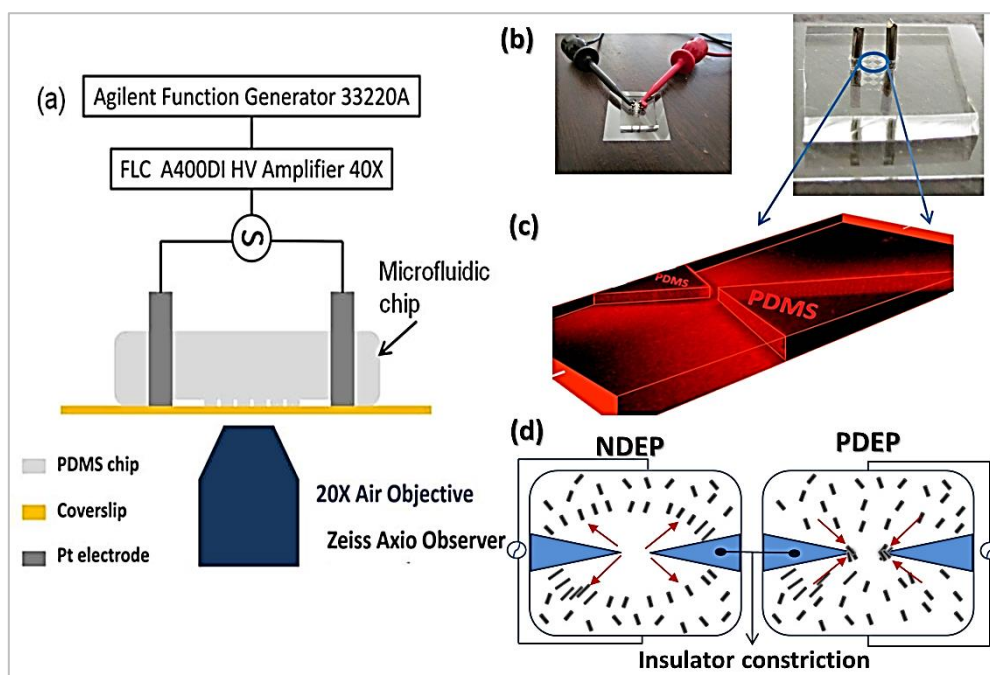


Figure 2.1: (a) Schematic device set-up; (b) Images of representative device; (c) confocal image of the constriction region. Trapping of particles in the constriction region under: (d) positive DEP (PDEP) and (e) negative DEP (NDEP).

The schematic set-up utilized for the DEP studies on the particles (*C. parvum* oocysts or *C. difficile*) is shown in **Figure 2.1**. Standard PDMS (Poly-di-methyl-siloxane) micro-molding methods were used to microfabricate a channel of ~ 1 cm length and $15 \mu\text{m}$ depth, with several sharp lateral constrictions from $1500 \mu\text{m}$ to $15 \mu\text{m}$ and back to $1500 \mu\text{m}$ over a total extent of $\sim 100 \mu\text{m}$ length (**Figure 2.1b**)¹⁷. This so-called “constriction chip” was bonded using a 1 minute oxygen plasma treatment to a standard glass coverslip for easy microscopic viewing of DEP behavior (**Figure 2.1a**). After filling the micro-channel with the samples, Pt electrodes were inserted and sealed within the “inlet” and “outlet” to activate the electric field. AC fields were applied using a function generator and a voltage amplifier for fields of ~ 300

V_{pp}/cm at a frequency range of 1 kHz to 15 MHz¹⁸. Under conditions for positive DEP (PDEP), the oocysts were translated towards the constriction tip (**Figure 2.1d**) and under negative DEP (NDEP) they were translated away from the constriction tip (**Figure 2.1e**).

Computing dielectrophoretic spectra from particle velocity measurements

For a particle accelerated under a dielectrophoretic force (F_{DEP}), based on Newton's second law, the net force on the particle of radius: a , within a medium of viscosity: η , can be determined by tracking displacement (x) as a function of time (t):

$$F_{DEP} = m \frac{d^2x}{dt^2} + 6\pi\eta a \frac{dx}{dt} \dots \text{Eq.(3)}$$

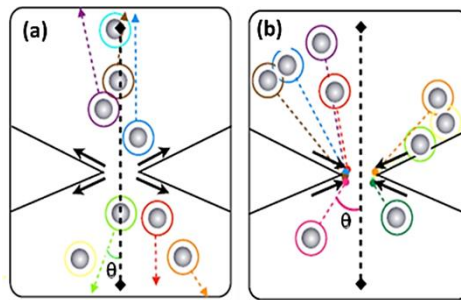


Figure 2.2: Translation vectors for particles under: (a) NDEP; and (b) PDEP.

The dielectrophoretic translation of particles is shown in **Figure 2.2**. Based on data from high frame per second (~ 30 fps) movies of particle translation under F_{DEP} , the displacement (x) is tracked as a function of time (t) for particles translated away from the constriction tip under negative DEP (NDEP) and towards the constriction tip under positive DEP (PDEP). For NDEP, the translation of particles that were originally at rest at the constriction tip is observed upon application of the AC field at a particular frequency of interest by recording their displacement, onwards from the constriction tip along a particular displacement vector over a particular time period (**Figure 2.2a**). For PDEP, the translation of particles that were

originally at rest in the region immediately outside of the constriction gradient is observed upon application of the AC field at a particular frequency of interest, by recording their displacement towards the constriction tip along a particular displacement vector over a particular time period (**Figure 2.2b**).

As a result we obtain velocity (dx/dt) for the particles at a particular applied field and frequency, which can be used to indicate the dielectrophoretic frequency response in the direction of the particle trajectory (“track” direction).

Image analysis on Electrode-based DepTech 3DEP reader

In the study of inhibitory effect of NTCD on HTCD in Chapter 4 section 2, we utilized a commercial electrode-based DepTech 3DEP reader (www.deptech.com), to obtain the DEP spectra.

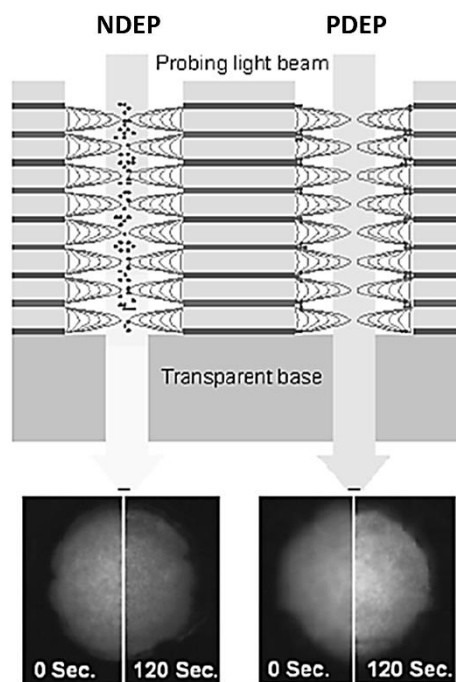


Figure 2.3 The electrodes are energized at a range of frequencies. Particles within the well show positive or negative DEP. The intensity of light passing through the well indicates the magnitude and sign of the force. (Adopted from Ref[18])

A schematic of DEP measurement by light adsorption is shown in **Figure 2.3**, as described in detail by Hoettges *et al*¹⁹. This device has been successfully applied to study yeast, cancer cells and neuronal stem cells¹⁹⁻²¹.

In the DepTech 3DEP reader, the DEP response is generated by applying different frequencies to 20 individual microfluidic DEP wells, so that the spectrum can be obtained by analyzing the light intensity from particle scattering within each of the 20 DEP wells. The internal area of each circular DEP well is divided to different regions by 10 concentric circles, so that there are 10 bands from the center to the edge of the well for analysis of light intensity. Specifically, the light intensity of each circular band in the well from the center to the edge is measured every 1 second, for a total of 30 seconds. Based on this, a 2D map of light intensity for different bands at different times is created by defining X-Axis as the radial distance from the center of the well and the Y-Axis as the time of measurement. This temporal map shows the light intensity at each band along the radius in the well from the center to the edge versus at each time point. Since the accumulation or depletion of particles causes a change in light intensity within different regions of the well, final light intensity at each point is normalized to the background (time = 0), where the field is not yet applied. In addition, since the electric field varies from the center to the edge, a weighting method for normalization of electric field is incorporated to correlate changes in light intensity at each of the different bands. As a result, the DEP force at each band can be compared²². Finally, these normalized weighted changes in light intensity are used to measure the relative DEP force at each frequency, as designated by a particular well.

For a high aspect ratio particle (major/minor axis), such as *C. difficile*, the particle undergoes electro-orientation as soon as the electric field is applied. Hence, in the 3DEP wells, once the field is applied, the high aspect ratio particles orient along the field lines. This means instead of random orientation, the major axis of the cells is rotated radially. This causes a dramatic and rapid accumulation in the light intensity in the well, which obscures all the light intensity

originating from DEP, since the subsequent light intensity is usually normalized to the intensity at time 0, thereby causing an incorrect spectrum indicating nDEP for most of the frequency range. Hence, in collaboration with engineers at DepTech's 3DEP reader, this problem was addressed by identifying the first frame following the electro-orientation of cells, and using this as the baseline for normalizing the light intensities from later frames.

Chapter 3

Dielectrophoretic characterization and separation of Cryptosporidium parvum

I. Quantitative Dielectrophoretic tracking for characterization and separation of persistent *Cryptosporidium parvum*

Introduction and Rationale

Need for sensitive quantification of subpopulations

Micro-organism samples are usually spread over developmental lifecycles and subpopulations, leading to their persistence due to altered levels of susceptibility to antibiotics^{4, 23}. The sensitive quantification of these heterogeneous modifications is a major challenge, especially for subpopulations with phenotypic rather than genotypic variations and for organisms that cannot be enriched in-vitro by microbial culture methods²⁴. The case of *C. parvum* illustrates this problem^{25, 26}. Ingestion of *C. parvum* oocysts, which are not deactivated by the standard chlorine treatments²⁷, leads to Cryptosporidiosis²⁸, which is estimated to be responsible for about 50% of the waterborne diseases attributed to parasites worldwide²⁹. On one hand, there is a need to sensitively quantify alterations to the oocyst by disinfectants, since as few as ten viable oocysts of the ~billion oocysts shed by a host during an infection episode³⁰, are sufficient to cause a new infection^{30, 31}. On the other hand, the heterogenous nature of the alterations during disinfection, due to subpopulations in the sample, leads to substantial variations in oocyst viability³².

Limitations of current methods

A relatively high concentration of $\sim 10^6$ oocysts/mL is required within in-vivo infectivity tests on animal models to enable quantitative assessments on modifications to oocyst viability³³. Additionally, the lack of means to proliferate the oocysts limits the sensitivity of in-vitro monitoring methods, since *C. parvum* oocysts typically only excyst and complete their lifecycle in the mammalian gastrointestinal tract. Biomolecular assessment of viability based on hsp70 mRNA levels is highly sensitive³⁴, but unsuitable for real-time monitoring during disinfection or in cases where subsequent analysis is needed on the oocysts. Hence, there is a need to separate and locally enrich oocyst subpopulations with particular alterations for quantification.

State of the art

Dielectrophoresis (DEP) technique has been applied to a wide range of cellular relevant studies, such as cellular characterization, manipulation and separation³⁵. Quantitative DEP characterization of cell electrophysiology can be accomplished through methods such as, measuring the DEP collection rate^{36,37}, determining the DEP crossover frequency of cells³⁸⁻⁴¹, measuring the DEP levitation height of cells⁴² or through actively tracking the translation of cells under DEP⁴³. However, a limitation within all these techniques is the lack of means to define the trajectory of the cells under DEP behaviour, especially under negative DEP. Hence, the data needs to be averaged over a large number of cells that are trapped over an ill-defined region of the device, thereby making them less sensitive to variations from small fractions of persistent subpopulations, such as: 10^{-5} - 10^{-6} of the total population for *E. coli*, that is phenotypically distinct and resistant to antibiotics⁴⁴.

Furthermore, although dielectrophoretic^{28, 29} and electro-rotation techniques^{30, 31} have been applied previously to investigate modifications to the oocyst wall of *C. parvum* after heat treatment, no prior work has quantitatively correlated the DEP behaviour to the modifications in structure and infectivity of sporozoites in the oocyst. This is necessary for the separation of oocysts based on sporozoite structure to discern the effectiveness of disinfectants, since infections are caused by the release of sporozoites from the oocyst.

Objectives

In this chapter, we aim to assess the utility of microfluidic DEP methods towards separation and characterization of disinfectant-induced alterations to *C. parvum*, by comparison to optical microscopy (fluorescence, phase and DIC contrast) for structural analysis and excystation and infectivity studies for functional analysis of the oocysts. Disinfection methods include two heat treatment methods: 90 C for 10 minutes and 70 C for 5 minutes, and several treatment approaches with silver nanoparticles (AgNP) of varying capping layers. AgNPs have been shown an enhanced antimicrobial effect over silver salts^{45, 46}, and have been widely investigated for water disinfection applications⁴⁷⁻⁵⁰.

Materials and methods

Preparation of *Cryptosporidium parvum* oocysts

Cryptosporidium parvum oocysts were purchased from Waterborne Inc. and stored at 4°C, until use. All the oocysts from a particular batch were used within a month, since oocysts undergo significant de-activation over time. The media conductivity (σ_m) of oocyst stock (10⁹/50 mL in phosphate-buffered saline) was lowered to 2 mS/m, by

centrifuging the oocysts (Eppendorf 5430), aspirating the supernatant and re-suspending the oocysts in DI water by vortexing to prevent aggregation or sedimentation.

Disinfection treatments on oocysts

For heat treatment, the oocysts were placed in a dry block/shaker (Thermomixer, Eppendorf) at 90°C for 10 minutes with 300 rpm shaking to allow homogenous heat distribution. An alternate treatment at 70°C for 5 minutes, which is the minimal level required for a loss of infectivity within the mouse model⁴⁷, was also studied for isolating persistent subpopulations with less intense modifications to the oocyst. For treatment with silver nanoparticles (AgNPs), the animal infectivity experiment was done after the oocysts were treated with 100 mg/L proteinate-capped AgNPs (Argenol) (~15 nm) and 100 mg/L polyvinylpyrrolidone (PVP)-capped AgNPs (nanoComposix) for 4 hours. While disinfection treatments were carried out over a 4 hour period, continuous DEP monitoring was used to confirm that steady state levels of oocyst deactivation were reached within 20 minutes for each treatment. For silver nitrate (AgNO₃) (Fisher Scientific) treatment, oocysts were treated with 100 mg/L AgNO₃ for 4 hours.

Fluorescence monitoring of oocysts

4',6-diamidino-2-phenylindole (DAPI) and propidium iodide (PI) were prepared in DI water to a stock concentration of 1 mg/ml by standard methods. The suspension of oocysts from each treatment was placed for 45 minutes in diluted DAPI (final concentration: 2 µg/ml) and then for 15 minutes in diluted PI (final concentration: 0.2 µg/ml). After an hour treatment with the fluorescent dyes, the oocysts were centrifuged, aspirated and re-suspended in DI water by vortexing to prevent any

aggregation and sedimentation. The wash steps were repeated twice to eliminate the background signal. Images were acquired using a Zeiss Observer Z1 microscope with a 63x oil immersion objective lens under bright field view for phase and Differential Interference Contrast (DIC) images, and fluorescent view for DAPI and PI images.

Excystation of oocysts and mouse model infectivity studies

After each disinfection treatment, the oocysts were treated with 10% bleach (Bleach-Rite) for 30 minutes in a micro-centrifuge tube at room temperature, followed by vortexing every 10 minutes. The suspension was incubated in a micro-vial chamber with a glass cover-slip for an hour, for real-time recording of the excystation; i.e. release of sporozoites from the oocyst. The excystation was examined under an inverted microscope using a 63x oil immersion phase and DIC objective lens. At least ten different fields of view were taken (Hamamatsu Orca Flash4) and results from at least 300 oocysts were used to calculate the net ex-cystation rate for each treatment. The percentage of the excystation was calculated as: ($\#$ of excysted oocysts / $\#$ of total oocyst) $\times 100^{29}$. For mouse model infectivity studies¹², all mice were malnourished for a period of 13 days before experiments. For every six mice fed with the oocysts for each treatment, three other mice were fed with untreated oocysts as positive control. RT-PCR analysis was performed on stool shed from mice from the day after inoculation to day 7, post-infection.

Results and Discussions

Identifying persistent subpopulations after disinfection

We begin with applying the excystation assay and infectivity tests on the mouse model to identify the persistent and sensitive subpopulations of *C. parvum* oocysts with differing phenotypic alterations after heat and AgNP treatment.

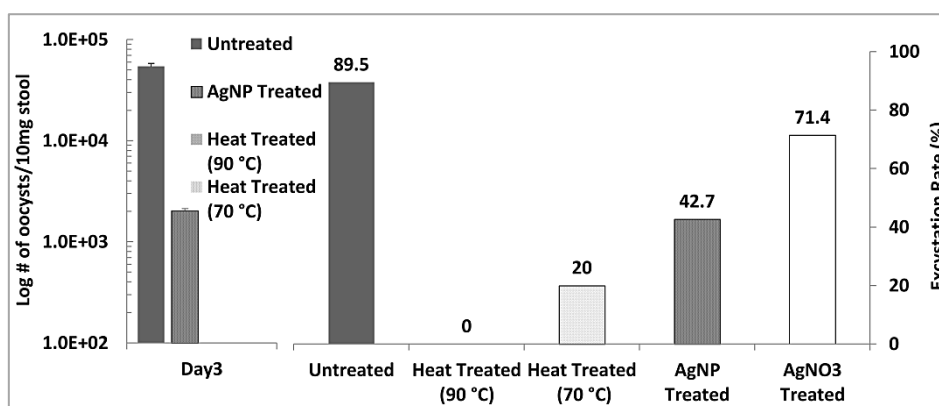


Figure 3.1 Functionality of sporozoites in the oocyst after disinfection treatments: (left) # of shed oocysts on day 3 of the infection on the mouse model; and (right) excystation rate. No oocysts shed after heat treatment.

As per **Figure 3.1 (left)**, based on # of oocysts shed from the mouse on Day 3 when the infection is most intense, as confirmed by the weight-loss data, the high infectivity of untreated oocysts is almost absent within heat treated oocysts at both, 90 C and 70 C. Following AgNP treatment, while the infectivity of the oocysts is significantly reduced, it is still discernible. Based on the excystation rate (**Figure 3.1 – right**), it is clear that while 89.5% of the untreated oocysts undergo excystation, the rate drops to 71.4% after AgNO₃ treatment, to 42.7% after AgNP treatment, and to 20% and 0%, after heat treatment at 70 C and 90 C, respectively. Together, these results suggest that while heat treatment of oocysts at 90 C causes complete de-activation, there are persistent subpopulations of inactivated oocysts after heat treatment at 70 C and after AgNP treatment. In comparison to AgNP treatment, the disinfectant effect of AgNO₃ is less significant, as apparent from the 70% excystation rate.

Heterogeneous modification of oocysts after disinfection

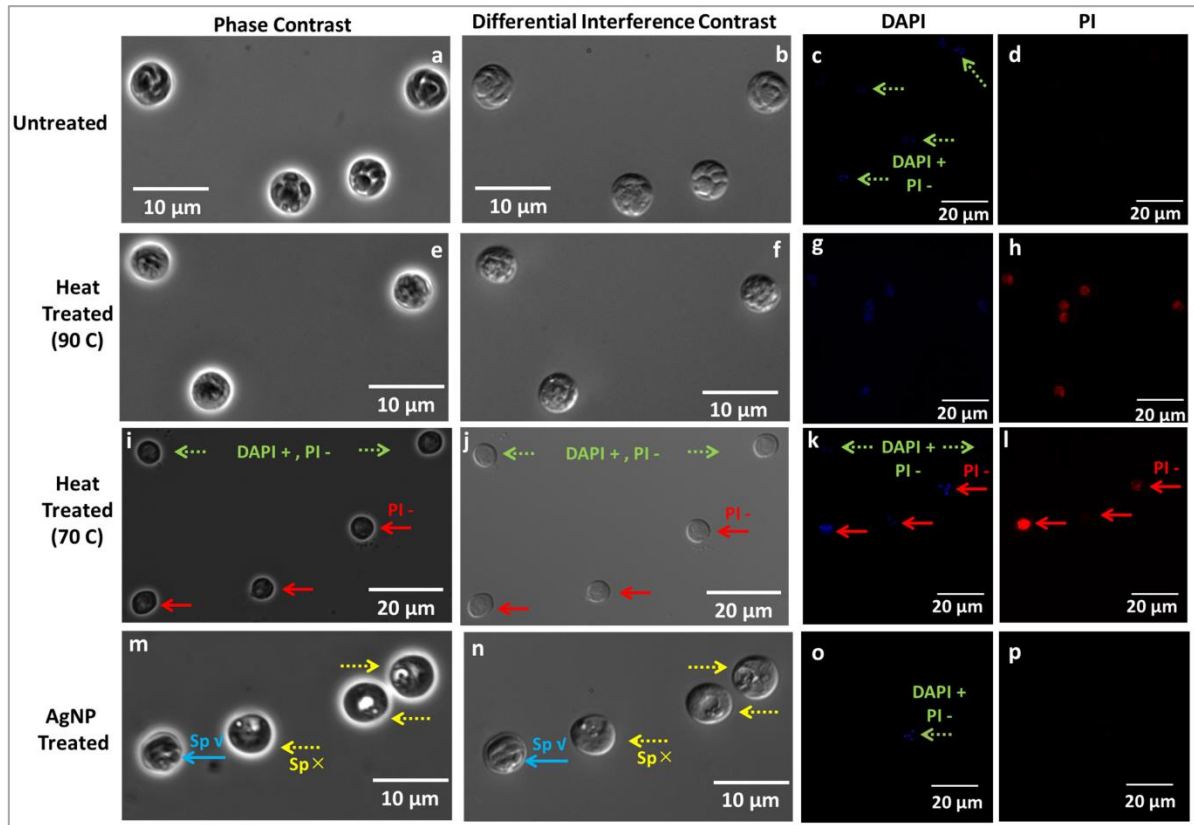


Figure 3.2 Microscopy of oocysts after various treatments: Column 1: phase contrast; Column 2: Nomarski Differential Interference Contrast (DIC); Column 3: DAPI fluorescence; Column 4: PI fluorescence; for: untreated (a – d); heat-treated at 90 C (e – h); heat-treated at 70 C (i – l); AgNP treated (m – p). Intact ($Sp \surd$) versus altered sporozoites ($Sp \times$) are confirmed by DAPI + (inclusion) and PI – (exclusion) (green arrows).

Viability of sporozoites in the oocyst can be indicated by the banana-shaped sporozoite morphology in phase and DIC microscopy modes, and the presence of DAPI signal in fluorescence mode, whereas absence of PI signal indicates integrity of the oocyst wall^{51, 52}. The distinct sporozoite structure of untreated oocysts is apparent in the phase contrast (**Figure 3.2a**), and DIC images (**Figure 3.2b**). Additionally, based on presence of DAPI labeling that delineates the four nuclei of the sporozoites (**Figure 3.2c**) and the absence of PI labeling (**Figure 3.2d**), henceforth labeled as: DAPI + / PI – (dotted green arrows), we infer

the viability of the oocysts. Note that for clarity, the phase and DIC images in **Figure 3.2** are at higher magnification than the fluorescence images. Heat treated oocysts at 90 C do not show a discernible banana-shaped sporozoite structure. Instead, a nebulous sporozoite structure that is indistinguishable from the background is apparent under phase contrast (**Figure 3.2e**) and DIC (**Figure 3.2f**), alongside a diffuse level of DAPI labeling that is spread beyond the four nuclei of the sporozoites (**Figure 3.2g**), suggesting a disorganized oocyst cytoplasm⁴⁹. Furthermore, the presence of PI labeling within the oocysts (**Figure 3.2h**), indicates disruption of the oocyst wall, henceforth labeled as: PI + (solid red arrows). Heat treated oocysts at 70 C indicate heterogeneous modifications, with a subpopulation showing intact sporozoites with DAPI + / PI – labeling and another showing the destroyed oocyst wall with PI + labeling (**Figure 3.2k and 3.2l**). The differential levels of PI signal from the PI+ labeled oocysts further indicates the heterogeneous modifications (**Figure 3.2l**). Upon AgNP treatment, instead of the banana-shaped sporozoite structure, the phase contrast image of the oocyst cytoplasm reveals a transparent region composed of a coalesced cluster adjoining an empty region (**Figure 3.2m**), with topographic differences in the DIC image (**Figure 3.2n**) that suggest an altered sporozoite structure. However, there is a small group of AgNP treated oocysts that continue to show the distinct sporozoite morphology of untreated oocysts, as apparent from the red arrow with Sp √ in **Figure 3.2m – 3.2n**. This sub-group of oocysts indicate the DAPI + / PI – signal delineating the nuclei of the sporozoites (**Figure 3.2o**), whereas the other sub-group of AgNP treated oocysts with the altered sporozoite structure (Sp ×) do not show any DAPI signal. The PI signal is uniformly absent from all AgNP treated oocysts (**Figure 3.2p**). Hence, optical microscopy confirms the heterogeneous modification of the oocysts after heat treatment at 70 C and after AgNP treatment. Note that these treatments were carried out over ~4 hours to ensure steady-state behavior. After heat treatment at 70 C, there is a persistent subpopulation with intact oocyst wall and sporozoite structure (DAPI + / PI –) and a sensitive subpopulation with a compromised oocyst wall and

diffuse sporozoite structure (PI +). After AgNP treatment, there is a persistent subpopulation with an intact sporozoite structure in the oocyst (Sp \checkmark) that indicates: DAPI + / PI – signal, whereas there is a sensitive subpopulation with an altered sporozoite structure in the oocyst (Sp \times), but with an intact oocyst wall (i.e. DAPI – and PI –). We infer that while optical microscopy is qualitatively consistent with excystation and infectivity assays, which indicate the partial loss of sporozoite functionality due to sensitive and persistent subpopulations after AgNP treatment and heat treatment at 70 C, these techniques are unable to quantify the degree of oocyst alteration and number of oocysts with a particular alteration.

Frequency-selective dielectrophoretic spectra

The DEP response of biological particles, such as *C. parvum* oocysts can be characterized using a shell model^{7, 35, 10}, with the shell composed of an oocyst wall of low conductivity ($\sigma_{\text{wall}} \sim 100 \text{ nS/m}$ as per⁵³) and a core of higher conductivity due to intact sporozoites within the cytoplasm ($\sigma_{\text{cyto}} \sim 0.05 \text{ S/m}$ ⁵³). The oocyst can be represented in terms of an equivalent circuit composed of a low-loss capacitor of capacitance: C , to denote the oocyst wall, in series with the high-conductivity oocyst cytoplasm of resistance: R . As per RC circuit analysis, at frequencies below the inverse RC time constant, the polarizability and net direction of particle translation is determined by the capacitor due to the oocyst wall, which should result in negative DEP (NDEP) behavior within moderately conducting media ($\sigma_m \sim 0.1\text{-}10 \text{ mS/m}$), due to: $\sigma_{\text{wall}} (\sim 100 \text{ nS/m}) < \sigma_m (0.1\text{-}10 \text{ mS/m})$ in Eq. (2). On the other hand, at frequencies above the inverse RC time constant, the high conductivity region at the oocyst core determines the DEP response, thereby causing positive DEP (PDEP) behavior, since: $\sigma_{\text{cyto}} (\sim 0.05 \text{ S/m}) > \sigma_m (0.1\text{-}10 \text{ mS/m})$ in Eq. (2). At very high frequencies ($\sim 10 \text{ MHz}$), the response is determined by permittivity rather than conductivity, which should cause NDEP behavior, due to: $\epsilon_{\text{cyto}} (\sim 60) < \epsilon_m (\sim 80)$ ⁵³.

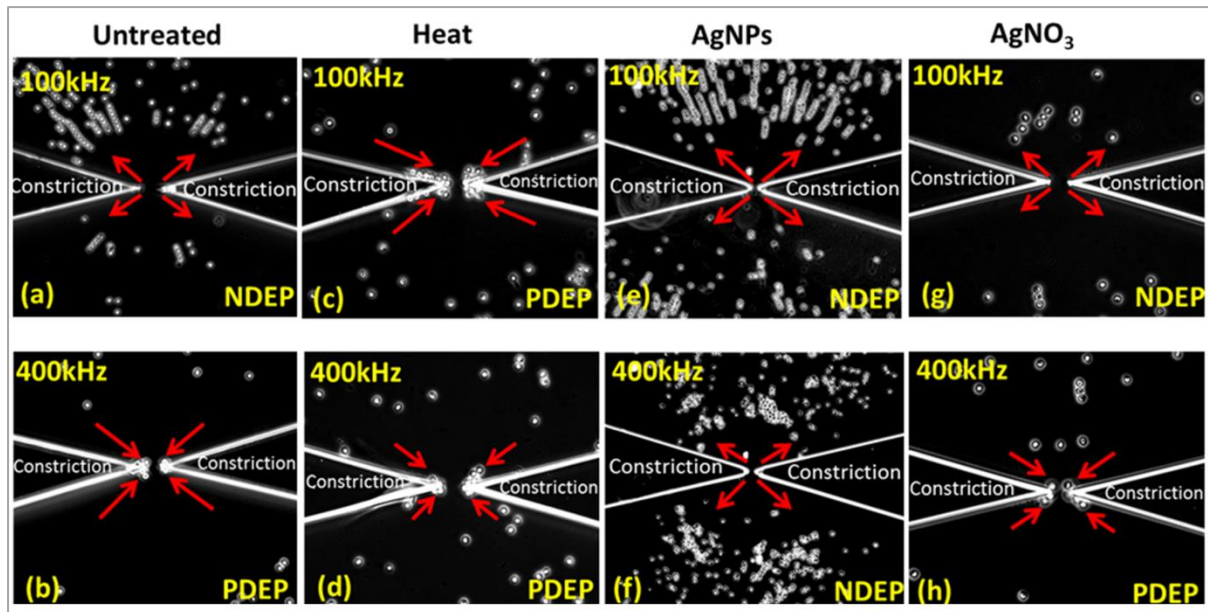


Figure 3.3 Dielectrophoretic behavior of oocysts in the constriction region after 30 seconds of AC field: 300 V_{pp}/cm at 100 kHz (a, c, e, g) or 400 kHz (b, d, f, and h), for: Untreated oocysts (a & b); Heat-treated (90 C) oocysts (c & d); AgNP treated oocysts (e & f); and AgNO₃ treated oocysts (g & h).

This is indeed the trend observed within **Figure 3.3**, which shows images in the vicinity of the insulator constriction region of the device after 30 seconds of the onset of DEP behavior at ~ 300 V_{pp}/cm field; and at frequencies of 100 kHz and 400 kHz, where the oocyst wall and the sporozoites in the oocyst cytoplasm, respectively, determine the net DEP behavior. For untreated oocysts, NDEP behavior occurs from 1 kHz onwards until ~ 200 kHz, as apparent from the strong translation force on the oocysts away from the constriction tip at 100 kHz (as per arrows in **Figure 3.3a**), whereas PDEP behavior occurs from 400 kHz onwards, as apparent from trapping of the oocysts at the constriction tip (as per arrows in **Figure 3.3b**). Upon heat treatment of the oocysts (90 C), the disruption of the oocyst wall, as apparent from the fluorescence images in **Figures 3.3g** and **3.3h**, affects the DEP response. The increased permeability of the oocyst wall impedes dipole formation across the oocyst

wall, thereby eliminating the screening action of the capacitor and the associated NDEP behavior. Instead, crossover to PDEP behavior is observed at earlier frequencies, due to polarization of the oocyst cytoplasm, which is no longer screened by the oocyst wall at low frequencies. Hence, the onset of PDEP, which occurs from 10 kHz onwards for heat-treated oocysts, is clearly apparent at 100 kHz in **Figure 10c**. At 400 kHz, PDEP behavior continues to be present, albeit at a significantly lower force level, as apparent from the fewer trapped oocysts at the constriction tip in **Figure 3.3d** after the same 30 seconds of applied field. Following AgNP treatment, the strong NDEP response is clearly apparent at 100 kHz in **Figure 3.3e**, indicating an uncompromised oocyst wall, which is consistent with the fluorescence results. At 400 kHz, instead of the oocysts being directed towards the constriction tips, as observed with untreated (**Figure 3.3b**) or heat treated oocysts (**Figure 3.3d**), the DEP force on AgNP treated oocysts continues to remain directed away from the constrictions tips (**Figure 3.3f**). However, the magnitude of the NDEP force at 400 kHz is lower versus that at 100 kHz, as apparent from localization of the oocysts closer to the constriction tip at 400 kHz (**Figure 3.3f**) versus 100 kHz (**Figure 3.3e**). For oocysts with an uncompromised wall, the DEP response at 400 kHz should be determined by the difference of cytoplasm and media conductivity. Hence, the NDEP behavior after AgNP treatment of the oocysts can be attributed to a reduction in the cytoplasm conductivity due to alteration of the sporozoites (σ_{cyto}), thereby obviating PDEP behavior, due to: $(\sigma_{\text{cyto}} - \sigma_{\text{m}}) < 0$. In the subsequent sections we explain the NDEP behavior of AgNP treated oocysts and correlate it to alteration of sporozoites in the oocyst. Finally, based on the similarity of DEP response of AgNO₃ treated versus untreated oocysts at 100 kHz (**Figure 3.3g**) and at 400 kHz (**Figure 3.3h**), we infer that the oocysts are not significantly altered, which is consistent with the excystation results.

To quantify DEP force from **Figure 3.3**, the particle acceleration and velocity can be determined by tracking the displacement of the oocysts versus time, and fit into the DEP force equation (Eq(3)). Details on this analysis can be found in the methodology section in Chapter 2.

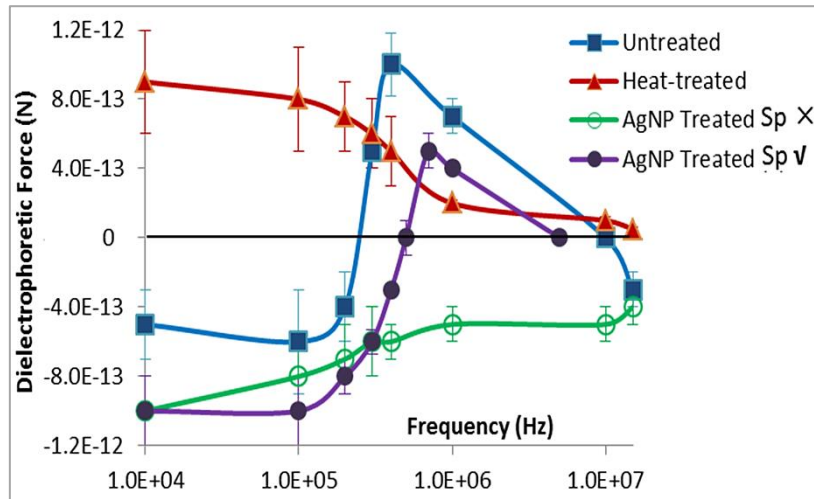


Figure 3.4: Measured F_{DEP} frequency responses from DEP tracking of Untreated and heat treated oocysts (90 C) at σ_m of 2 mS/m and AgNP treated oocysts at σ_m of 10 mS/m. Error bars are based on velocity profiles from 20 oocysts after each treatment type.

Figure 3.4 shows the frequency response of F_{DEP} (symbols) for untreated, heat treated (90 C) and AgNP treated oocysts. For untreated oocysts, the transition from NDEP behavior at low frequencies (<100 kHz) to PDEP behavior at mid-level frequencies (>400 kHz) is apparent. For heat treated oocysts, PDEP behavior starts at successively earlier frequencies, due to loss of the field screening by the compromised oocyst wall. For AgNP treated oocysts, we are able to identify different DEP behavior at frequencies beyond 400 kHz for sensitive oocysts with altered sporozoites (Sp \times) versus persistent oocysts with intact sporozoites (Sp \surd), as will be described in the subsequent section.

Separation based on oocyst wall and sporozoite infectivity

Finally, using the quantitative force response in **Figure 3.4** from the DEP tracking measurements, we can identify the appropriate frequency for effectively separating the sensitive versus persistent subpopulations of *C. parvum* after AgNP and after heat treatment (70 C), by utilizing differences in the magnitude and direction of the DEP trapping force. This is necessary, since persistent subpopulations can form extremely small fractions of the total population⁴⁶. Through collection rate measurements on the separated subpopulations, the fraction with a particular electrophysiological alteration or phenotype can be quantified.

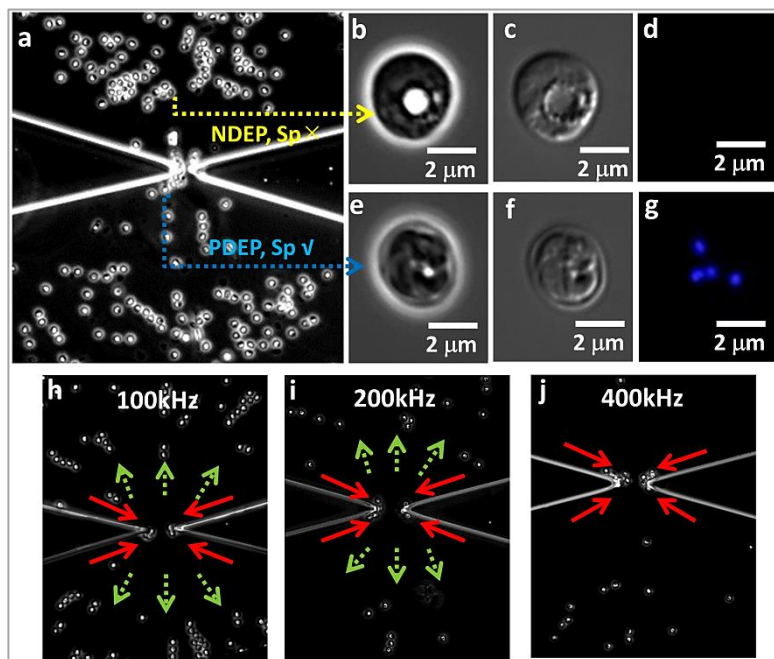


Figure 3.5 Dielectrophoretic separation of oocysts based on sporozoite alteration (a – g) and oocyst wall integrity (h – j). (a) 300 V_{pp}/cm field at 700 kHz causes NDEP of oocysts with altered sporozoites ($Sp \times$), as confirmed by absence of sporozoite structure in phase (b) and DIC images (c), and absence of DAPI signal (d). Oocysts with intact sporozoites ($Sp \surd$), as confirmed by presence of characteristic sporozoite structure in phase contrast (e) and DIC images (f), and the presence of DAPI signal (g) show PDEP trapping. (h) Separation based on oocyst wall integrity is more effective under 300 V_{pp}/cm field at 100 kHz, versus at: (i) 200 kHz, and (j) 400 kHz.

For oocysts with altered ($Sp \times$) versus intact sporozoites ($Sp \surd$) after AgNP treatment, a frequency of 700 kHz causes PDEP behavior for $Sp \surd$ oocysts (blue arrows), whereas $Sp \times$ oocysts experience NDEP behavior (yellow arrows), as per **Figure 3.5a**. Optical microscopy of the sub-group of AgNP treated oocysts exhibiting NDEP behavior confirms their altered

sporozoites (Sp ×), as apparent from absence of the banana-shaped sporozoite structure in the phase contrast (**Figure 3.5b**) and DIC images (**Figure 3.5c**), as well as the exclusion of DAPI signal in fluorescence images (**Figure 3.5d**). On the other hand, the oocysts exhibiting PDEP behavior show the distinct banana-shaped sporozoite structure in the high-magnification phase contrast (**Figure 3.5e**) and DIC (**Figure 3.5f**) images; as well as the presence of DAPI signal in fluorescence images (**Figure 3.5g**).

Next, we demonstrate the separation of the sub-groups with intact versus compromised oocyst walls, after heat treatment at 70 C. As per Figure **3.5h-3.5j**, a lower frequency of 100 kHz, where dominance of the screening action of the oocyst wall causes NDEP behavior, is more effective at separating the respective oocyst groups versus at higher frequencies, where the net polarization behavior of the oocysts is no longer sensitive to the oocyst wall. Oocysts with uncompromised walls exhibit NDEP up to 200 kHz, whereas those with disrupted walls exhibit PDEP, starting from successively lower frequencies (depending on degree of disruption) and extending to ~400 kHz. Hence, judicious choice of the frequency can enable more effective separations through modulation of the magnitude and direction of the DEP trapping force.

II. Dielectrophoretic characterization of silver nanoparticle induced disinfection action on oocysts of *Cryptosporidium parvum*: Effect of nanoparticle functionalization

Introduction and Rationale

The surface capping layer stabilizing silver nanoparticles (AgNPs) affects their aggregation, dissolution, and net disinfection action⁴⁶. For example, the disinfection action of electrostatically stabilized citrate capped AgNPs is attributed to generation of reactive oxygen species (ROS) rather than Ag⁺, whereas steric stabilized AgNPs by protein- or starch-capping arrests ROS generation due to interferences from the bulky capping layer, so that

Ag⁺ release kinetics determine disinfection action. In our previous work, we have quantified the influence of silver ion (Ag⁺) release and reactive oxygen species (ROS) generation rates for AgNPs of varying surface functionalization on their net disinfection action on *Escherichia coli*⁴⁶. In the results of Part I in this chapter, we demonstrated the disinfection action of proteinate-capped AgNPs on *C. parvum* oocysts, based on alterations in dielectrophoretic response that were correlated to their sporozoite structure and substantiated by considerable reductions in infectivity. Herein, we seek to compare the influence of polyvinylpyrrolidone (PVP)-capped AgNPs versus proteinate-capped AgNPs on their disinfection action on *C. parvum* oocysts, as judged by electrophysiology due to sporozoites, and correlate versus the alterations to the mouse infectivity model, *in vitro* excystation behavior and morphological characteristics.

Results and Discussions

Effect of AgNPs capping layer on their morphological modifications to oocysts

We begin with examination of the morphological differences of *C. parvum* oocysts after each disinfectant treatment. Oocysts of *C. parvum* were observed under high resolution phase contrast and Nomarski differential interference contrast (DIC) microscopy before and after disinfectant treatments, including heat, PVP-capped AgNPs, proteinate-capped AgNPs and AgNO₃ treatments. Phase contrast microscopy of untreated oocysts using a high resolution phase objective and camera reveals the transparent oocyst wall and four intact sporozoites arranged in a banana-shape, as apparent in **Figure 3.6a**. The DIC image of the untreated oocysts in **Figure 3.6b** provides topographic evidence for the presence of intact sporozoites.

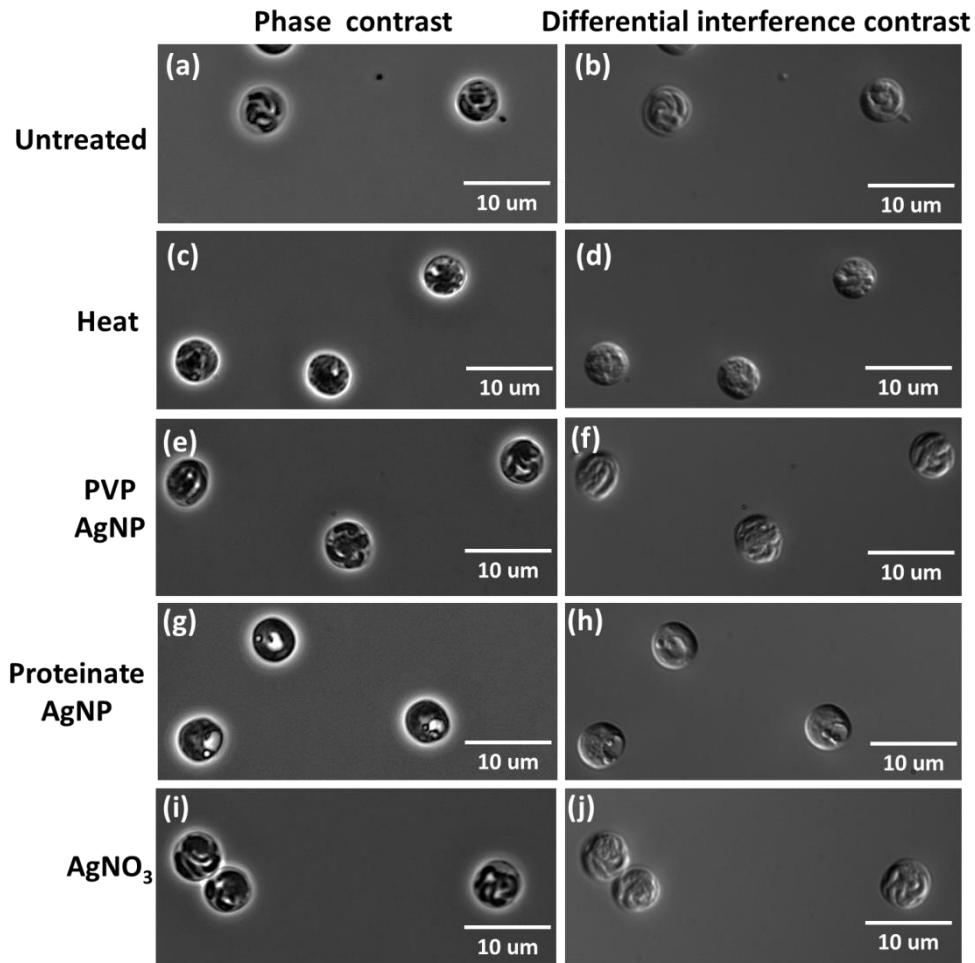


Figure 3.6: High resolution contrast images illustrating the morphological differences in the oocysts after disinfectant treatments. First column shows phase contrast images and second column shows Nomarski differential interference contrast images under different treatments: (a and b) Untreated; (c and d) Heat-treated; (e and f) PVP-capped AgNP treated; (g and h) Proteinate-capped AgNP treated; (i and j) AgNO₃ treated oocysts of *Cryptosporidium parvum*.

It is noteworthy that while optical microscopy is not a certain means for characterizing intact sporozoites, due to the limited magnification and poor contrast, the batch to batch variations in the number of intact sporozoites per oocyst can be reduced by imaging over multiple focal planes⁵⁴. Upon heat treatment, instead of the distinct banana-shaped arrangement of the sporozoites, the oocyst cytoplasm is filled with nebulous undistinguishable structures, as apparent in the phase contrast image (**Figure 3.6c**), while the DIC image also reveals a disorganized sporozoite structure in the oocyst (**Figure 3.6d**). Following treatment with

PVP-capped AgNP, the sporozoites bear some degree of resemblance to the banana-shaped arrangement that is observed within untreated oocysts (**Figure 3.6e and f**). Following treatment with proteinate-capped AgNP, the banana-shaped arrangement of the sporozoites is no longer detectable. Instead, the oocyst cytoplasm in **Figure 3.6g** reveals a coalesced cluster that seems transparent in the phase contrast image adjoining an empty region, suggesting an altered sporozoite structure. The DIC image (**Figure 3.6h**) shows the smooth surface of the big cluster, with a clear topographic difference between the cluster and the empty region. However, there is a small group of the proteinate-capped AgNP treated oocysts that continue to show the sporozoite morphology of untreated oocysts (data not shown). Finally, following AgNO₃ treatment, the oocysts continue to show sporozoites arranged in a banana-shape (**Figure 3.6 i and j**), as observed within the untreated oocysts.

Effect of AgNPs capping layer on their modifications to the excystation behavior of oocysts

Oocysts of *C. parvum* usually excyst only within mammalian gastro-intestinal systems. However, *in vitro* excystation can occur in the presence of appropriate conditions, such as promoted by exposure to bleach solution, resulting in thinning of the oocyst wall for exposing the receptors on the oocyst wall, thereby causing the sporozoites to secrete parasite-derived enzymes that set off signal transduction towards excystation. This excystation process is similar to that causing infectivity of the oocysts within mammalian gastro-intestinal systems. Since only viable and infective oocysts exhibit excystation^{13, 55}, we used the excystation behavior of the oocysts before and after the disinfection treatments as a means to test viability of sporozoites and their infectivity.

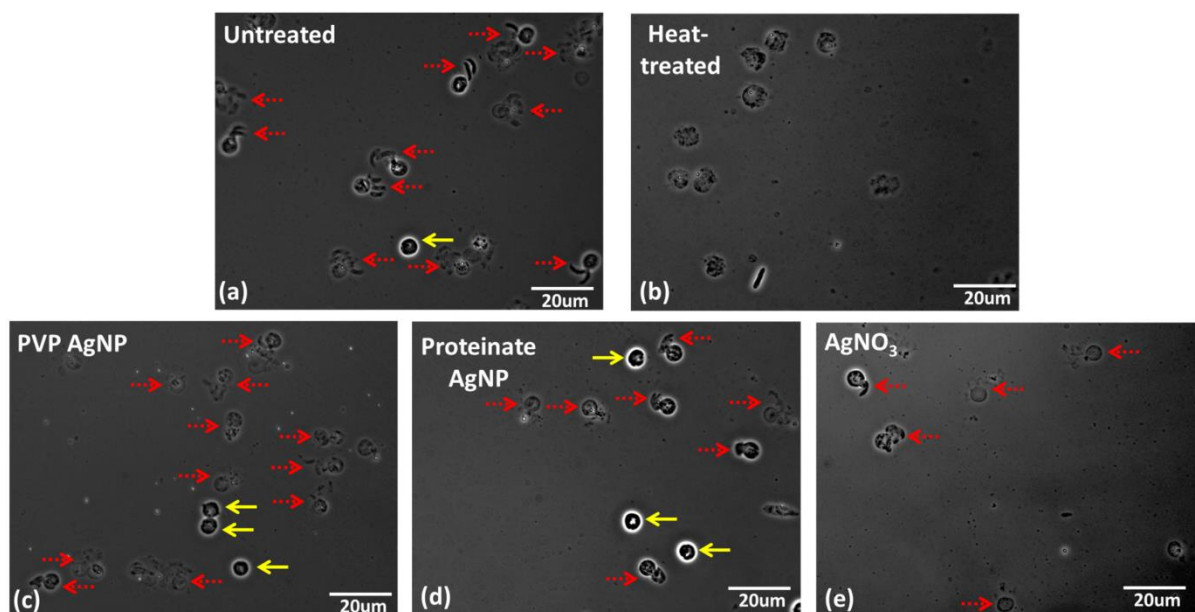


Figure 3.7: Typical images from excystation studies on the oocysts: (a) Untreated; (b) Heat-treated; (c) PVP AgNP treated; (d) Proteinate AgNP and (e) AgNO₃ treated oocysts of *C. parvum*. Dotted arrows (red) shows excystation behavior of the oocysts and solid arrows (yellow) shows the lack of excystation behavior of the oocysts.

As per **Figure 3.6a**, the banana-shaped sporozoites of untreated oocysts are released under conditions of 10% bleach solution. The excystation rate is ~90%, as apparent from the red dotted arrows versus a few stray cases of oocysts not exhibiting excystation, as apparent from the yellow solid arrow, which are likely due to aged or degraded oocysts⁵⁴. Upon heat treatment, the oocyst undergoes a significant level of disruption, as was apparent in **Figure 3.6c and 3.6d**. The parasite-derived enzymes and proteins that set-off excystation undergo denaturation and loss of functionality⁵⁶, thereby causing the loss of excystation behavior. Following treatment of the oocysts with PVP-capped AgNPs, the banana-shaped sporozoites are mostly intact as in **Figure 3.6e and 3.6f**, and these exhibit excystation (**Figure 3.7c**) at a ~80% rate. A few of the oocysts do not show excystation, which may be attributed to the aged or degraded set of oocysts, or to the subpopulation of oocysts that is vulnerable to the disinfectant. Following treatment with proteinate-capped AgNPs, since the banana-shaped sporozoites are no longer apparent in the oocysts (**Figure 3.6g and h**), these oocysts do not exhibit excystation as indicated by the yellow solid arrows in **Figure 3.7d**. On the other hand,

other oocysts with intact sporozoites do show excystation, thereby causing a net ~40% excystation rate for proteinate-capped AgNP oocysts. Finally, AgNO₃ treated oocysts, continue to show presence of banana-shaped sporozoites (**Figure 3.6i and 3.6j**) and up to 90% excystation rate (**Figure 3.7e**).

Frequency-selective dielectrophoretic spectra of each AgNP capping layer

We next utilize DEP to examine the mechanism of each AgNP capping layer treatment. We choose the frequencies of 100 kHz and 400 kHz, where the oocyst wall and the sporozoites in the oocyst cytoplasm, respectively, determine the net DEP behavior, as previously described.

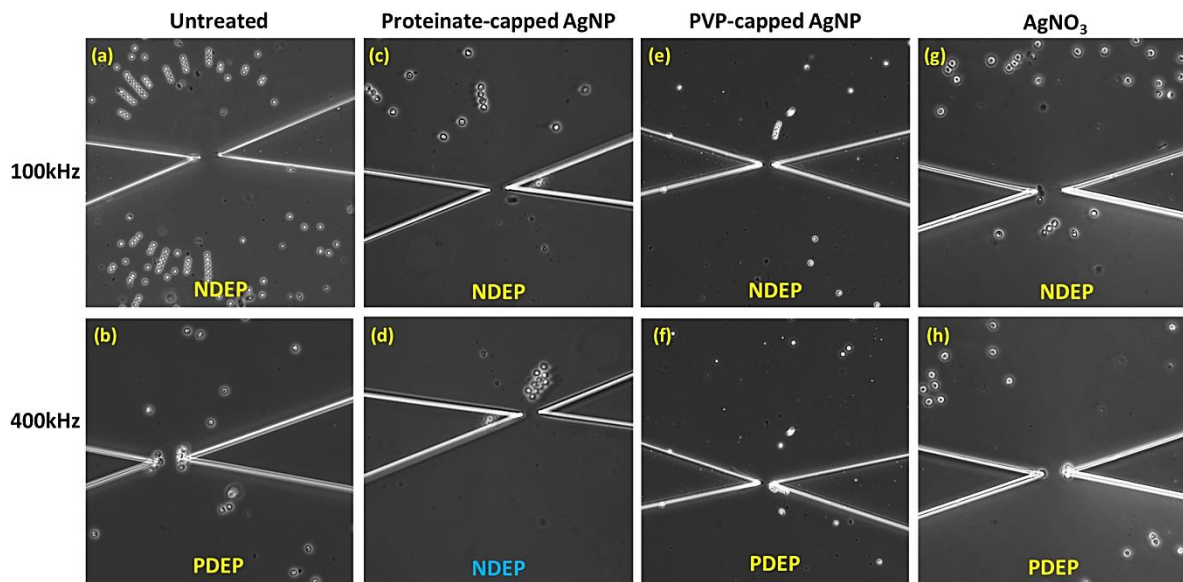


Figure 3.8 Dielectrophoretic behavior of oocysts in the constriction region after 30 seconds of AC field: 300 V_{pp}/cm at 100 kHz (a, c, e, g) or 400 kHz (b, d, f, and h), for: Untreated oocysts (a & b); Proteinate-capped AgNPs treated oocysts (c & d); PVP-capped AgNPs treated oocysts (e & f); and AgNO₃ treated oocysts (g & h).

The untreated oocysts show NDEP behavior at 100kHz, apparent from the strong translational force on the oocysts away from the constriction tip as shown in **Fig. 3.3a and 3.8a**), whereas the untreated oocysts show PDEP at 400 kHz, as apparent from trapping of the oocysts at the constriction tip as shown in **Fig. 3.3b and 3.8b**. The proteinate-capped AgNPs treated oocysts continue to show NDEP at 100 kHz (**Figure 3.8c**), which indicates an

uncompromised oocyst wall. However, instead of showing PDEP at 400kHz as seen in untreated (**Figure 3.8b**), the oocysts show NDEP behavior, which suggests a reduced cytoplasm conductivity due to an altered cytoplasm (**Figure 3.8d**). This alteration in cytoplasm electrophysiology can be correlated to the altered sporozoite in the cytoplasm as was shown based on altered sporozoite morphology (**Figure 3.6 g and h**), reduced excystation rate (**Figure 3.7d**). For the PVP-capped AgNPs (**Figure 3.6e and f**) and AgNO₃ (**Figure 3.6g and h**) treated oocysts, on the other hand, the same DEP response as untreated oocysts is observed, indicating unmodified oocyst wall and sporozoites in the cytoplasm. The unchanged oocyst electrophysiology after treatment with PVP-capped AgNPs also corresponds to the intact oocyst morphology (**Figure 3.6 e and f**), and high excystation (**Figure 3.7c**).

Effect of AgNPs capping layer on their disinfection action on mice model

Finally, we confirm with infectivity tests on the mouse model to identify the disinfection of oocysts by each type of functionalization on AgNPs. This mouse model data was collected at Dr. Guerrant's lab within the Infectious Diseases department by former graduate student, Lydia Abebe (Advisor: James Smith). The oocysts numbers are collected from stool samples at day 2 and day 3 following the infection of the mouse with *C. parvum* and quantified by PCR. As per **Figure 3.9**, the infectivity is most intense in the untreated group and is almost absent within the heat-treated group, where the shedding is well below the detection limit. For the AgNPs treated groups, the PVP-capped AgNP treatment does not show the loss of infectivity, whereas the infectivity is significantly reduced in the group of oocysts treated with proteinate-capped AgNPs. Finally, the AgNO₃-treated group also shows some decrease in infectivity, with more significant loss of infectivity at day 3.

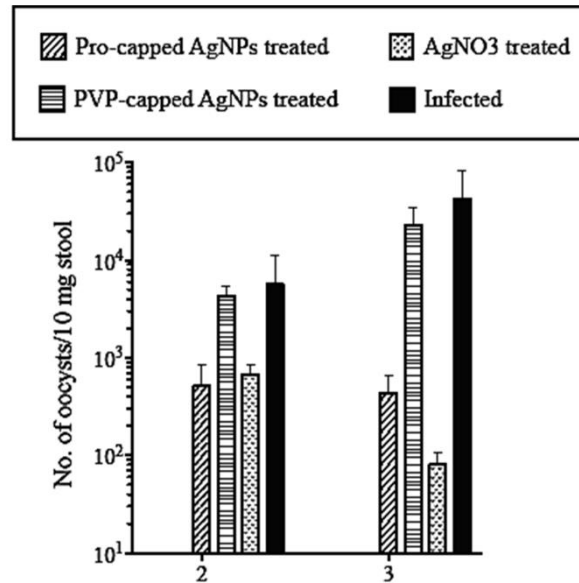


Figure 3.9 *C. parvum* oocyst concentration in stool shed from mice as a function of post infection time for different oocyst disinfection treatments. Each data set represents a different oocyst disinfection method as well as positive (infected) and negative (uninfected) controls. Error bars represent standard error for each measurement. *Heat treated group not represented in graph, shedding was below detectable limit. (This mice experiment is done by Lydia Abebe in Prof. James Smith’s group)

III. Conclusions

Towards quantifying persistent microbial subpopulations with phenotypically different alterations after disinfection treatments and characterizing their alterations, we demonstrate the utility of quantitative dielectrophoretic tracking for force measurements over a wide frequency range (10 kHz – 10 MHz). Utilizing a device with insulator constrictions to localize the field and modulate the spatial extent of the field gradient so that it is symmetric across the device depth, we are able to establish a well-defined trajectory of cells under positive and negative dielectrophoresis. As a result, the simultaneous and facile tracking of velocity of individual cells can be accomplished for computing the quantitative force response, which is more sensitive to electrophysiological differences from subpopulations, since there is no need for averaging over large collection regions. This quantitative force

response over the 10 kHz – 10 MHz frequency range is applied to characterize and separate sensitive versus persistent subpopulations that were identified by excystation and animal infectivity assays during the disinfection of *C. parvum*. Through correlating the force response at 0.4-1 MHz to integrity of sporozoites in the oocyst and at ≤ 100 kHz to the integrity of the oocyst wall, we demonstrate the separation of persistent subpopulations after AgNP treatment and heat treatment at 70 C, respectively.

We utilized DEP methods to demonstrate the differences in disinfection action of AgNPs of varying capping layers through correlation against the mouse infectivity model, in vitro excystation and optical imaging of the morphological characteristics of the sporozoites. Disinfection treatments based on PVP-capped AgNPs do not significantly alter the banana-shaped arrangement of the sporozoites in the oocyst, which is consistent with their high ex-cystation rate and continued infectivity determined using the model, while their strong pDEP response onward from 400 kHz confirmed the maintenance of a conductive cytoplasm electrophysiology due to intact sporozoites and their nDEP response at low frequencies (100 kHz) confirmed an uncompromised oocyst wall. However, while AgNO₃ treatment of the oocysts showed a significant reduction of infectivity within the mouse model, the complementary methods showed an intact sporozoite morphology, high excystation rates and DEP responses that were similar to those of untreated oocysts. One possible reason for this discrepancy may arise from the differences in duration of the treatment times, since AgNO₃-treated oocysts likely take longer time to alter the oocysts, as apparent from the significant loss of infectivity only on Day 3 of the treatment (**Figure 3.9**). Treatment with proteinate-capped AgNPs alters the banana-shape arrangement of the sporozoites within the oocyst, without affecting the oocyst wall, accompanied by a significant drop in the excystation rate to ~40%, and these observations correspond to the alteration of DEP spectra compared to untreated.

In the current state of the art, the electrode-less DEP have been applied towards separation and discrimination of different microbial samples, but only DC fields have been used⁵⁷⁻⁵⁹, which limit the potential for monitoring the differences and alterations in both: cell membrane and cytoplasm. With DC, this can only be done by changing the media conductivity, which is cumbersome and impractical. The current work represents the first demonstration of quantitative DEP spectra over a wide frequency range using an electrode-less DEP device for characterizing disinfection of microbials. In this manner, we are able to quantify the disruption mechanisms of different disinfectant by examining the permeability of the membrane at low frequency and the integrity of sporozoites in the cytoplasm at high frequencies. This is especially important as biological particles have complicated internal structures, and we can obtain more information from the crossover frequencies by applying AC fields in a wide frequency range. We envision the application of this technique for probing subtle distinctions in microbial electrophysiology after immuno-magnetic separation from large water systems, and this label free method can also be used for optimizing AgNPs formulations to enhance disinfection treatments for *C. parvum*.

Chapter 4

Dielectrophoretic characterization and separation of Clostridium difficile

I. Independent dielectrophoretic monitoring and separation of individual *Clostridium difficile* strains based on their S-layer proteins

Introduction and Rationale

Clostridium difficile infection (CDI) is a toxin-mediated intestinal disease that is commonly attributed to exposure to pathogenic *C.difficile* strains following the elimination of healthy microflora in the gut, due to administration of antibiotics⁶⁰. Prior studies within animal models strongly suggest that asymptomatic colonization with non-toxigenic *C.difficile* (NTCD) strains can reduce the incidence of CDI from toxigenic *C.difficile* (TCD) strains⁶¹⁻⁶³, and this preventive effect is substantiated within a meta-analysis of four studies on hospitalized patients⁶⁴, as well as a phase 1 study that has confirmed the ability of NTCD strains to colonize the GI tracts of healthy human subjects pretreated with vancomycin⁶⁵. All of this has led to much interest towards reducing the incidence of CDI through pre-colonization with NTCD strains.

Limitations of current methods

The development of such preventive therapies against CDI requires means to monitor NTCD colonization during antibiotic and other therapeutic interventions, so that the antagonistic interactions between differing strains during co-infection can be characterized and optimized. However, there is no independent way to simultaneously monitor physiological alterations in

both, NTCD and TCD strains, especially during antibiotic and therapeutic interventions. The gold standard of CDI diagnosis is culture of the bacteria from stool samples and testing for toxin production levels (cytotoxicity assay)⁶⁶. Given the time-consuming nature of toxigenic *C.difficile* culture, rapid diagnosis of CDI is usually accomplished by enzyme immunoassays (EIA) that can directly identify TCD strains through detecting the glutamate dehydrogenase (GDH) levels, as well as that of toxin A (TcdA) and/or toxin B (TcdB) levels. However, this method is hampered by poor sensitivity due to rapid degradation of the toxins⁶⁶, thereby requiring its combined application with a PCR assay to reduce false-positives and false-negatives^{66, 67}. Furthermore, colonization by NTCD strains cannot be monitored by EIAs due to absence of the toxins, or by PCR-restriction fragment analysis of the pathogenicity locus (PaLoc)^{60, 68} due to absence of the PaLoc within NTCD strains. Hence, there is a need for methods to simultaneously monitor the levels and physiological alterations of each *C.difficile* strain within a mixed microbial sample, preferably in a label-free, non-destructive and real-time manner.

Objectives

Dielectrophoretic (DEP) frequency spectra are highly dependent on the morphology and phenotype of microbials, with characteristic features that can indicate strain level differences^{57, 58, 69}. The objectives of this current work include: (a) distinction of toxigenic versus non-toxigenic *C.difficile*, as well as human hypervirulent versus non-hypervirulent clinical isolates strains by correlating their phenotype to particular features on their DEP spectra; (b) benchmarking alterations in the DEP spectra after antibiotic treatment against conventional measures of *C.difficile*, such as the immunoassay for toxins and their growth rate; (c) Characterizing antagonistic interactions of NTCD to TCD strains using DEP spectra in conjunction with the immunoassay for toxins and growth rate studies; and (d) Exploring

methodologies for the isolation of TCD and NTCD endospores.

Material and Methods

***C.difficile* sample preparation**

All experiments were conducted in a biosafety level 2 (BSL2) certified laboratory. The *C. difficile* samples (purchased from ATCC) were transferred into the microfluidic chip within the biosafety cabinet and sealed with platinum electrodes to prevent leakage. The dielectrophoretic motion of the respective *C. difficile* cells under the external field can then be observed under the microscope, outside of the biosafety cabinet, since the well-sealed device obviates exposure. Following imaging, the chip was disposed as per standard BSL2 procedures. In some cases, the trapped cells were collected for measurements of cell viability and the supernatant was collected to identify toxigenic versus non-toxigenic strains using the toxin immunoassay. The *C.difficile* strains were cultured in brain heart infusion (BHI) broth (BD BBL Brain Heart Infusion) at 37°C overnight under anaerobic conditions, before further antibiotic treatment or dielectrophoresis experiments. The overnight cultured bacteria suspension (250 µL) and 750 µL of the BHI with vancomycin (Novaplus) or without vancomycin (for the control groups) were mixed in Eppendorf tubes and incubated at 37°C for 4 hours or 24 hours. The vancomycin concentration for VPI10463 (high-toxigenic, HTCD) was 2mg/mL and 1 mg/mL for ATCC630 (low-toxigenic, LTCD) and VPI11186 (non-toxigenic, NTCD). Prior to the dielectrophoresis experiments, the BHI broth was replaced with 8.8% sucrose water and re-adjusted with BHI broth to optimize the medium conductivity $105 \pm 5\%$ mS/m for enabling DEP-based distinction of *C.difficile* strains from mixed samples. All three strains were confirmed to be viable within this altered BHI media over the timeframe of the DEP experiments, as per the colony forming unit (CFU) assay (see supporting information).

Adhesion assay

Based on prior work^{70, 71}, the human colon epithelial cell line, HCT-8 (purchased from ATCC) was used as the host cell in this assay. The HCT-8 cells were cultured in RPMI medium supplied with 10% horse serum, 1 mM sodium pyruvate, and 100 U/mL penicillin and 100µg/mL streptomycin at 37°C in a 5% CO₂ incubator. Cells were grown as a confluent monolayer in 6-well plates prior to the assay. PBS and RPMI-serum free medium were pre-reduced for oxygen removal by overnight incubation in the anaerobic chamber. Before the adhesion assay, the cells were washed twice with PBS and replaced to RPMI-serum free medium. Overnight *C.difficile* cultures were pelleted and re-suspended in fresh BHI medium to avoid any interference from proteins or toxins. All three *C.difficile* strains were adjusted to equal concentration by optical density measurement. An equal concentration of each *C.difficile* strain was added to each well and the plates were incubated in the anaerobic chamber at 37°C for 3 hours. After 3 hours, non-adhered *C.difficile* cells were eliminated by three wash steps with PBS. Following this, 1mL PBS was added to each well, and the cells were scraped, vortexed, serially diluted and plated to enumerate adherent *C.difficile* colony-forming units (CFU). Each experiment was performed in triplicate, and repeated at least three times in entirety. All standard deviations (*SD*) in this study are obtained by using:

$$SD = \sqrt{\frac{\Sigma(x - \bar{x})^2}{(n - 1)}} \dots [1]$$

Growth measurement

Overnight cultured *C.difficile* suspension (250 µL) and 750 µL of the BHI broth, with or without vancomycin were mixed in Eppendorf tubes. The optical density at a wavelength of 600nm (OD600) of the mixed bacteria suspensions, as measured by Spectrophotometry (Eppendorf Biophotometer) before incubation, was indexed as the “0 hour” time point. The

OD600 number at later incubation time points (4 and 24 hours) for the respective strain at each condition was normalized to its 0 hour point. Each experiment was performed in triplicate, and repeated at least three times in entirety.

Toxicity enzyme-linked immunosorbent assay

Total toxin (A/B) production was measured using the *C.difficile* TOX A/B II kit (Tech- Lab) according to the manufacturer's instructions. Culture supernatants were collected at 0, 4 and 24 hours by centrifugation at 3500 rcf for 5 min and stored at -20 °C. The supernatants of the VPI10463 strain were diluted 1 to 20, while the supernatants of the VPI11186 strain were undiluted. Each specimen was run in duplicate. Total toxin levels were determined by measuring A450 under a 96 well plate spectrophotometry. The A450 number at each time point (4 hours and 24 hours) for each strain at each condition was normalized to its 0 hour time point. Each experiment was performed in triplicate, and repeated at least three times in entirety.

Sample preparation for transmission electron microscope imaging

C.difficile samples cultured overnight (1 mL) were pelleted and fixed in 2% glutaraldehyde and 2% paraformaldehyde in PBS for 4 hours at room temperature. The samples were pelleted and washed 3 times in DI water before re-suspension in 2% osmium tetroxide. After 30 minutes, the samples were pelleted and washed 2 times in DI water before the dehydration process. The samples were dehydrated through a serial gradient ethanol solution (50%, 70% 95% and 100%), for a 10 minute for each sample. The samples then re-suspended in 1:1 EtOH/EPON (epoxy resin) overnight, followed by 1:2 EtOH/EPON for 2 hours and 1:4 EtOH/EPON for 4 hours and 100% EPON for overnight. After embedding the samples in fresh 100% EPON, the samples were baked in a 65 °C oven. The EPON hardened samples

were sectioned to 75 nm, mounted onto 200 mesh copper grids and contrast stained with 0.25% lead citrate and 2% uranyl acetate for TEM imaging (JEOL 1230) at 80 kV (SIA digital camera).

Dielectrophoretic characterization of *C.difficile*

The experimental setup has been described in our prior work^{1, 17}. Briefly, standard PDMS (Poly-di-methyl-siloxane) micro-molding methods were used to microfabricate channels with sharp lateral constrictions (1000 μm to 15 μm). This so-called “constriction chip” was bonded using oxygen plasma treatment to a standard coverslip for easy microscopic viewing of DEP behavior. Using Pt electrodes at the inlet and outlet, AC fields were applied over a wide-frequency range (50 kHz-5 MHz) by utilizing a power amplifier for particle trapping towards or away from high field points at the constriction tips. The trajectory of the unlabeled *C.difficile* of each strain type was observed under this field, as high frame per second movies to quantify the DEP velocity. The data acquisition was automated to enable the capture of movies at each frequency within about ten seconds, with the entire frequency spectrum completed within about 5 minutes. The same cells could be measured multiple times under the DEP field since we used the electrode-less DEP technique under high frequency AC fields, with applied fields less than 300 $\text{V}_{\text{pp}}/\text{cm}$, thereby obviating electro-permeabilization effects, which we confirmed through viability analysis on microbials under the DEP field. For experiments within mixed *C.difficile* samples, the trapped microbials were released and the supernatant was analyzed with the immunoassay to confirm toxigenicity. The DEP analysis was conducted on the microbials following the log phase stage of their culture period, to ensure the insensitivity of DEP analysis to the temperature of the culture media and time for the culture. A full description of the simultaneous and automated dielectrophoretic tracking of single bio-particles can be found in our previous work.¹

Results and Discussions

Morphological differences between *C.difficile* strains

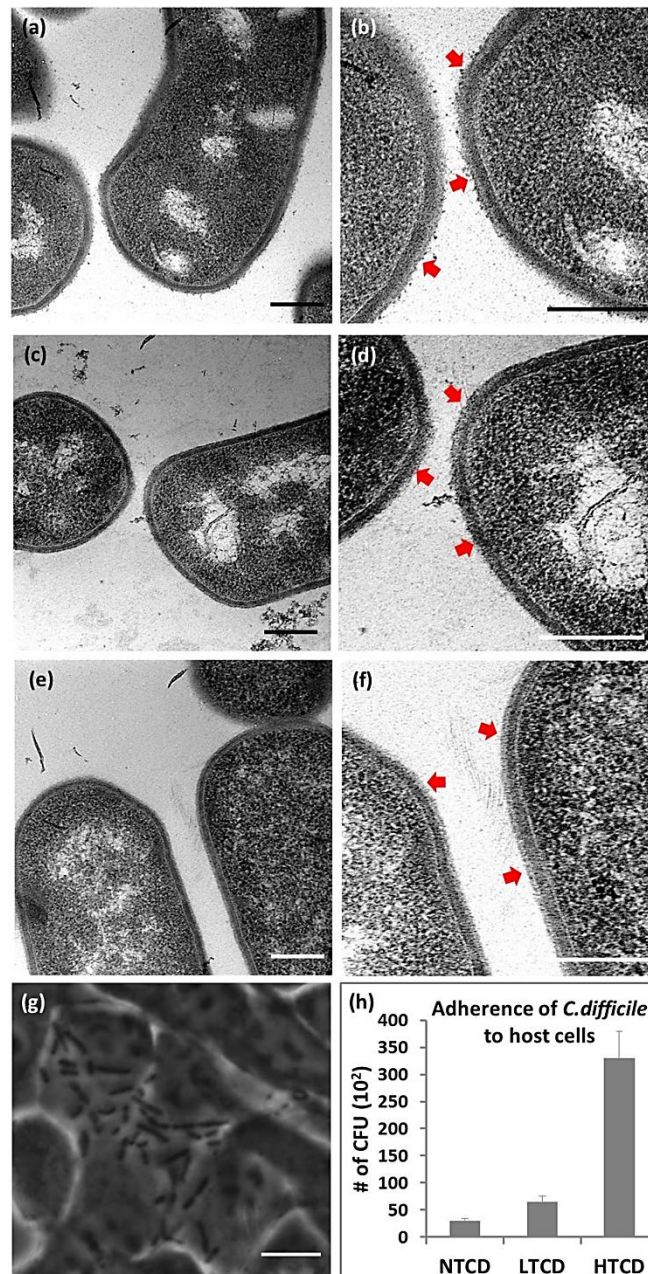


Figure 4.1 Transmission electron microscope images of the *C. difficile* strains at 50k magnification (a, c and e) and 100k magnification (b, d and f). All TEM scale bars are 0.2 μm . (a & b): HTCD (High-toxigenic *C.difficile*, VPI10463); (c & d): LTCD (Low-toxigenic *C.difficile*, ATCC630) and (e & f): NTCD (non-toxigenic *C.difficile*, VPI11186) strains. (g): A representative phase contrast image showing HTCD adherence to the human colon epithelial host cells. Scale bar: 5 μm . (h) Variations in adherence of each *C. difficile* strain to human colon epithelial cells by enumerating colony-forming units (CFU).

We begin with an examination of the morphological differences between three particular *C.difficile* strains: the high-toxigenic VPI10463 strain (HTCD), the low-toxigenic strain ATCC630 (LTCD) and the non-toxigenic strain VPI11186 (NTCD). While the chief difference between NTCD and TCD strains is lack of the PaLoc sequence⁷², particularly the TcdE holin-like membrane protein which signals the release of toxins, in addition to TcdA and TcdB, the other major difference is the S-layer proteins on their cell wall, which exhibit sequence variations^{67, 73}. Specifically CwpV, the largest of the cell wall protein (CWP) family, varies significantly among different strains of the same *C.difficile* species⁷⁴. As per the Transmission Electron Microscopy images at 50k magnification in **Fig. 4.1 (a, c and e)** and at 100k magnification **Fig. 5.1 (d, d and f)**, the three *C.difficile* strains show systematic variations in surface roughness in the cell wall region adjoining the membrane, which may be attributed to their S-layer proteins⁷⁵. The cell wall region of the HTCD strain has rough and spike-like features (**Figure 5.1a and 5.1b**), whereas features of the NTCD strain are relatively smooth (**Figure 5.1e and 5.1f**), with features of the LTCD strain being in between those of the HTCD and NTCD strains (**Figure 5.1c and 5.1d**). It has been demonstrated that the S-layer protein deficient bacteria show much smoother cell surface⁷⁵, which implies that the HTCD strains have highest abundance of S-layer proteins based on their high cell wall roughness and surface area, followed by the LTCD strain and then by the NTCD strain, which exhibits relatively smooth surface features. One of the chief differences between the

respective strains is the S-layer on their cell wall, which exhibits *SlpA* gene and *Cwp* gene sequence variations.^{67, 73, 74} Based on prior observations of a smoother cell surface for the S-layer deficient mutant *Tannerella forsythia* versus the wild type,⁷⁵ we seek to correlate the inter-strain morphological differences in *C.difficile* to their S-layer variations, by using a standard adhesion assay. It has been shown that surface layer proteins are the chief determinant for the adherence of *C.difficile* to host cells⁷¹ and for binding to gastrointestinal tissues⁷⁶. **Fig. 4.1g** shows a representative phase contrast image of the adherence of HTCD to the human colon epithelial host cells after three wash steps. As per **Fig. 4.1h**, the HTCD strain shows the strongest adherence to the host cells, followed by LTCD and finally NTCD strains. This correlation of high cell wall roughness of the *C.difficile* strain-type to its enhanced host-cell adherence suggests an abundance of S-layer proteins within the HTCD strain, with successively lower S-layer protein levels within the LTCD and NTCD strains due to their relatively smoother features and poorer adhesion to the host cells. We also note that the average cell wall thickness of the HTCD strain (32.1 ± 3.8 nm) is lower than that of the NTCD strain (38.3 ± 5.2 nm), as averaged over 10 cells, as per the measurements in **Figure 4.2**.

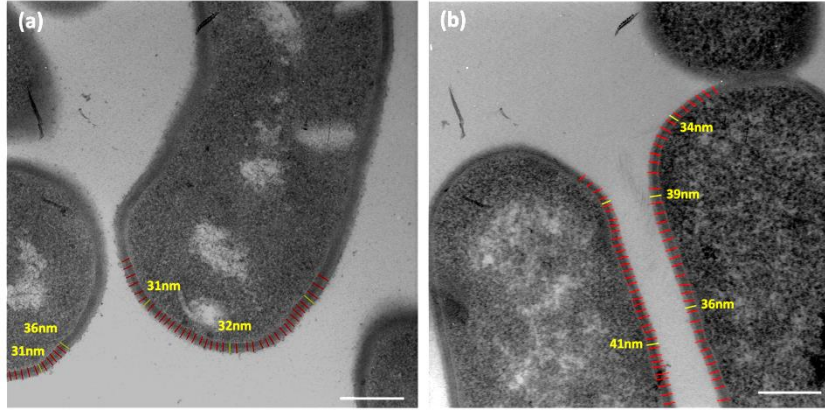


Figure 4.2 The representative measurements of cell wall thickness images of (a) HTCD with an average of 33.2 ± 4.1 nm; and (b) NTCD with an average of 36.9 ± 4.3 nm. Note the out-of-focus regions are not analyzed in order to avoid any ambiguous measurements. Scale bar: 200 nm

Independent dielectrophoretic monitoring of each *C.difficile* strain

Dielectrophoresis (DEP) of biological particles, such as *C.difficile*, can be characterized using a shell model^{77, 78}. Herein, the net capacitance (C) due to the dielectric properties of the cell wall and membrane screens the electric field at low frequencies to cause NDEP, whereas the low resistance (R) due to conductive properties of the cytoplasm dominates at high frequencies to cause PDEP, with the crossover frequency from NDEP to PDEP being determined by the inverse of the RC time constant due to the net resistance and capacitance of the system. Since the capacitance rises linearly with surface area (A), as per **Eq. (4)**, using a parallel-plate capacitor model for the cell wall with spacing: d , and material permittivity: ϵ , changes in surface roughness and area of the cell wall would cause systematic differences in the net capacitance of each *C.difficile* strain.

$$C_{net} = \epsilon A/d \dots \mathbf{Eq. (4)}$$

Based on this, the DEP crossover frequency (f_{xo}) for each *C.difficile* strain can be related to these differences in net wall and membrane capacitance (C_{net}) at a given media conductivity (σ_m), as follows⁷⁹:

$$f_{xo} = \frac{\sigma_m}{\sqrt{2\pi r C_{net}}} \dots \mathbf{Eq. (5)}$$

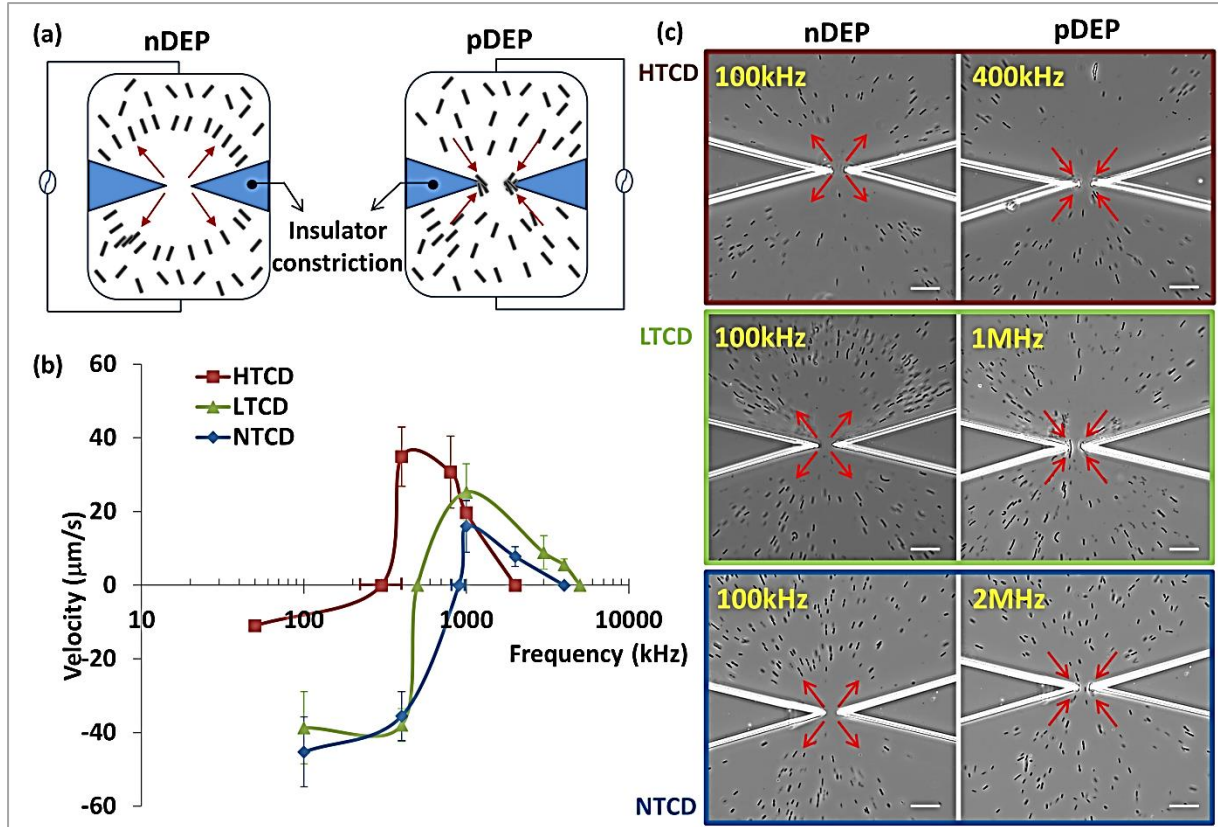


Figure 4.3 (a) Well-separated Dielectrophoretic spectra (velocity under F_{DEP}) for HTCD (high-toxigenic *C.difficile*, VPI10463), LTCD (low-toxigenic *C.difficile*, ATCC630) and NTCD (non-toxigenic *C.difficile*, VPI11186) strains; (b) Dielectrophoretic behavior of each *C.difficile* strains in the constriction region after 30 seconds of AC field: 300 Vpp cm^{-1} of negative DEP (left column) at 100 kHz for all three strain or positive DEP (right column) at 400 kHz, 1 MHz and 2 MHz for HTCD, LTCD and NTCD, respectively.

Hence, based on the higher net capacitance for the HTCD strain versus the NTCD strain, with the respective value for LTCD strain lying in between the two, we anticipate the lowest f_{xo} for the HTCD strain, followed by that of the LTCD strain and finally the NTCD strain. However, in order to observe this systematic difference in f_{xo} between the three strains, it is necessary to optimize the media conductivity (σ_m). Below a critical value of σ_m , the high resistance of the surrounding media will dominate the net RC time constant of the system, thereby driving the f_{xo} to low values and making it insensitive to differences in wall capacitance between the three strains. On the other hand, above a critical σ_m value, PDEP cannot be effectively observed (PDEP requires particle conductivity to exceed media conductivity), thereby posing

complications towards determination of the f_{xo} , due to lack of a clear crossover. This requirement for conducting DEP within media of a substantial conductivity level to enable the observation of differences in the f_{xo} between *C.difficile* strains, poses a challenge due to the disruptive effects of electrolysis and electro-permeabilization of cells within electrode-based DEP devices at substantial σ_m values. Hence, in this current work, the influence of these disruptive effects on DEP observations is eliminated by the use of electrode-less devices, where cell trapping under DEP does not occur at the electrode, but instead at or away from the tips of insulator constrictions that are designed to locally enhance electric fields. This electrode-less device geometry also enables facile and automated dielectrophoretic tracking due to the well-defined particle trajectories (either towards or away from highly localized constriction tips) and a symmetric field profile across the device depth. In this manner, as per prior work¹, the translational velocity under the DEP trapping force is measured for ~20 individual microbial cells to quantify the DEP spectra. Upon optimization of σ_m at: 100 mS/m range, well separated DEP spectra for each strain are apparent, as per **Figure 4.3**. Example images in vicinity of the constriction region of the device after 30 seconds of ~300 V_{pp}/cm field at the optimal frequency for NDEP and PDEP behavior are shown in **Figure 4.3c** for each strain, with arrows to denote the direction of translation and the respective velocity values at each frequency are reported in **Figure 4.3b**. Based on this, while nDEP is highest at 100 kHz for all strains, the highest PDEP occurs at distinctly different frequencies of: 400 kHz, 1 MHz and 2 MHz for HTCD (VPI10463), LTCD (ATCC630) and NTCD (VPI11186) *C.difficile* strains, respectively. This successively higher crossover frequency for LTCD and NTCD strains versus the HTCD strain is consistent with their progressively lower net wall capacitance due to lower surface area, as per the TEM images in **Figure 4.1**. Furthermore, based on successive reduction of the magnitude of maximum positive DEP force levels for HTCD to LTCD to NTCD strains, we infer a gradual reduction in cytoplasm polarizability for the respective strains. Finally, it is apparent that in

spite of the reduction in cytoplasm polarizability for the NTCD strain versus others, a discernible level of positive DEP can be observed up to ~ 4 MHz with the NTCD strain, up to ~ 2 MHz with the LTCD strain and up to ~ 1 MHz with the HTCD strain. We envision that these characteristic spectral features in the 0.1-5 MHz range can offer the means to separate the three strains from each other and from other microbial species within heterogeneous samples.

Alterations to each *C.difficile* strain upon vancomycin treatment

Alterations to the electrophysiology of cells upon antibiotic treatment, such as distinguishing the degree of cell wall permeabilization versus cytoplasm disruption, can be quantified by analyzing the dielectrophoretic frequency spectra of treated versus untreated cells¹. Herein, we utilize DEP to probe relative differences in the mechanism of microbial disruption for each *C.difficile* strain after vancomycin treatment, especially since similar measurements based on toxin production and growth rate can only indicate the altered functionality after vancomycin treatment, without providing information on the disruption mechanism, i.e. to the membrane or cytoplasm. Furthermore, DEP spectra can offer information on the optimal frequencies for separating vancomycin treated cells from untreated cells of each *C.difficile* strain, thereby enabling a means for quantifying the efficacy of vancomycin treatment on each strain, especially within heterogeneous samples.

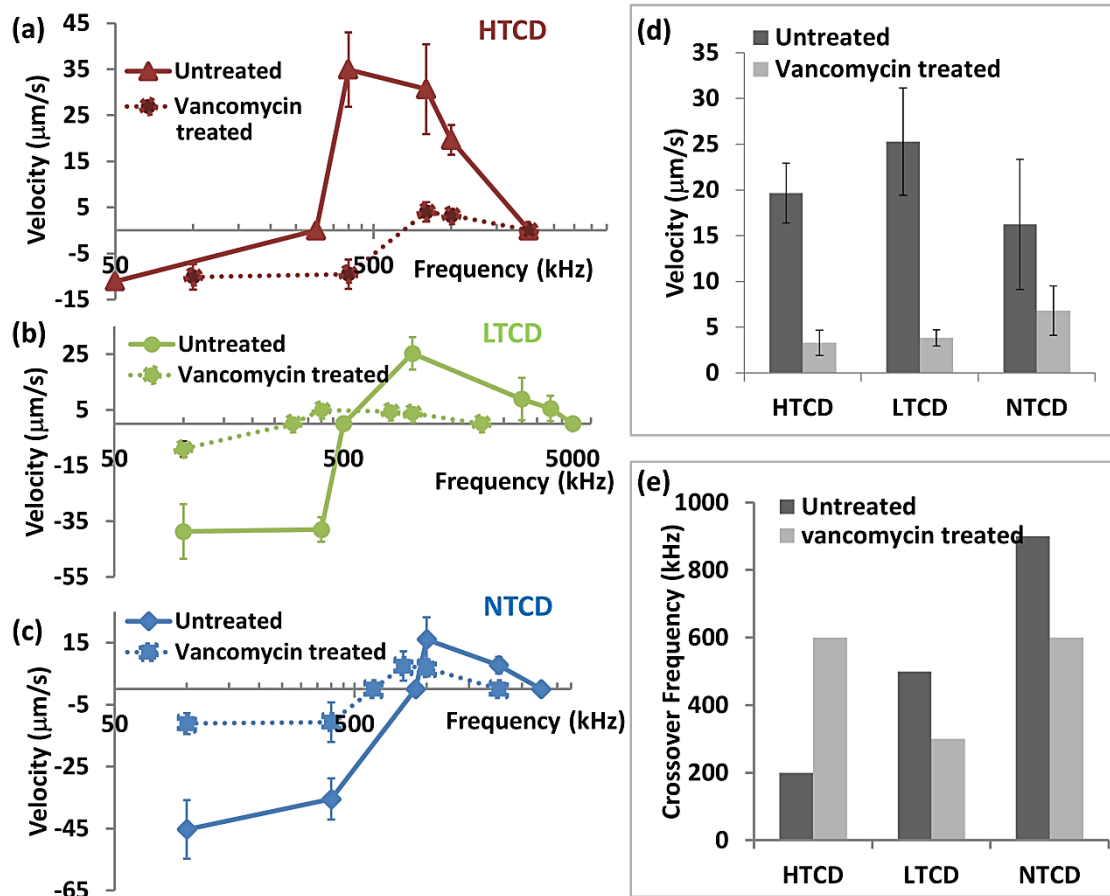


Figure 4.4 (a-c) Modification of Dielectrophoretic spectra (velocity under Dielectrophoretic force) can be used to monitor alterations after vancomycin treatment of (a) HTCD, (b) LTCD and (c) NTCD; (d) The alteration of the magnitude of the DEP response (velocity under Dielectrophoretic force) after vancomycin treatment at 1MHz; (e) The change of crossover frequency after vancomycin treatment.

In general, all the three strains become less polarizable due to functionality alterations to the cell after 24 hours of vancomycin treatment. However, the HTCD strain requires almost twice as much vancomycin levels than required for LTCD and NTCD strains to cause alterations to the DEP spectra. As a result of vancomycin treatment, while the DEP spectra for the HTCD strain (**Figure 4.4a**) is shifted towards a higher crossover frequency (200 kHz to 600 kHz); the spectra for the LTCD strain (**Figure 4.4b**) and the NTCD strain (**Figure 4.4c**) are shifted towards successively lower crossover frequencies (500 kHz to 300 kHz for LTCD and 900 kHz to 600 kHz for NTCD). To quantify the relative alterations after vancomycin treatment, we show the steady reduction in DEP velocity for each strain at 1 MHz (**Figure 4.4d**) and the

changes in crossover frequencies (**Figure 4.4e**). It is likely that vancomycin treatment alters the permeability of the cell wall and membrane, so that the lowered inverse RC time constant of the system enables DEP crossover at earlier frequencies, as observed for the NTCD and LTCD strains. For the HTCD strain, on the other hand, the need for higher vancomycin levels to cause alterations and the up-shifting of the DEP crossover frequency after vancomycin treatment suggests a relatively sturdier cell wall and membrane that is not easily permeabilized, in comparison to the LTCD and NTCD strains. This is somewhat consistent with prior observations that infer the need for higher antibiotic levels to deactivate HTCD strains versus others⁸⁰.

Benchmarking DEP velocities to toxin production and growth rate

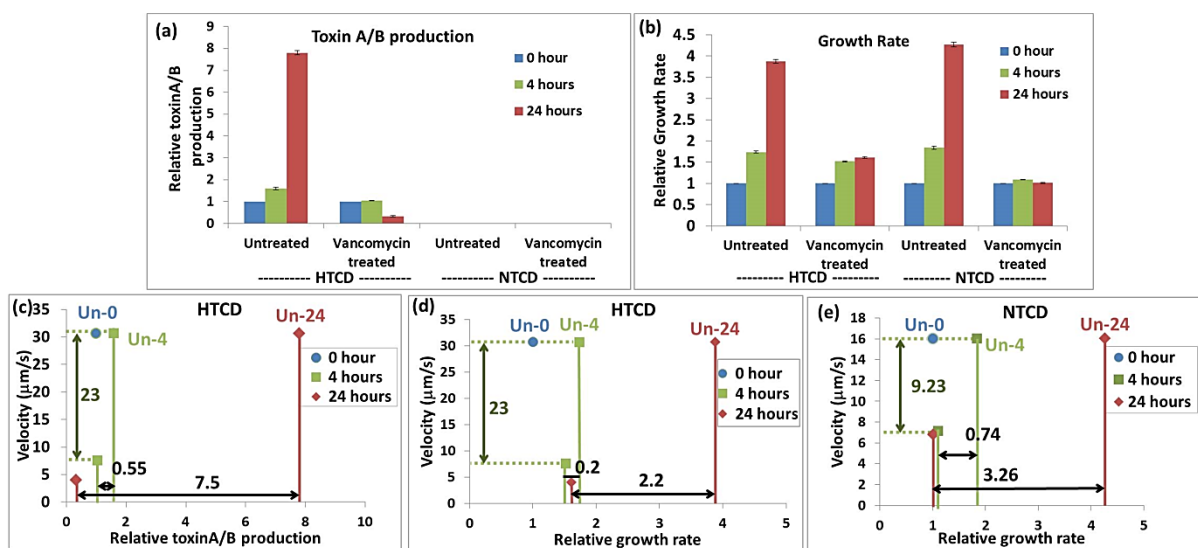


Figure 4.5 (a) Relative toxin production and (b) relative growth rate for HTCD and NTCD strains before and after vancomycin treatment at 0, 4 and 24 hours. The data points after 4 hours and 24 hours of treatment are normalized to their respective value at the 0 hour time point. The differences in microbial toxin production (c for HTCD) and growth rate (d for HTCD & e for NTCD) after vancomycin treatment are compared versus the control (0 hour treatment) as arrows in X-direction, while the alterations in DEP response after each treatment are shown as arrows in the Y-direction. Note that the respective control value for the Untreated sample at various time points is shown as: Un-0, Un-4 and Un-24 (controls are invariant over treatment time for DEP data but not so for toxin production and growth rate data).

In order to evaluate the sensitivity of DEP methods versus the current state of the art, we benchmark the DEP velocity data for HTCD and NTCD *C.difficile* strains after various levels of antibiotic treatment versus conventional diagnostic measures for the loss of *C.difficile* functionality, such as toxin production and growth rate values. To compare DEP data across the *C.difficile* strains, we choose the 1 MHz frequency, since all untreated strains show an equal level of pDEP, and the respective vancomycin treated samples continues to show pDEP. For measuring alteration in toxin production level and growth rate of *C.difficile* strains after antibiotic treatment, it is necessary to culture the microbial cells with the antibiotic over a period of 4-24 hours, to enable sufficient sensitivity. Hence, these results on the untreated or antibiotic treated microbials are reported as a proportion of their respective value versus that after a “0 hour culture time” (indexed as “1”). Furthermore, the results after antibiotic treatment for a particular period of time are compared against their respective values on untreated microbials for the same period of culture time (this control value for each treatment time is indicated as “Un-0”, “Un-4” or “Un-24” in Fig. 4c-4e). On the other hand, since DEP velocity measurements do not require microbial culture to enhance sensitivity, the “control” measurement for DEP velocity of untreated *C.difficile* is invariant with antibiotic treatment time. **Figure 4.5a** shows the steady exponential rise in toxin production levels with culture time for the untreated HTCD strain, while the alterations upon vancomycin treatment lead to only a mild rise (1.05 times) after 4 hours of treatment and a small reduction after 24 hours treatment, due to degradation of residual toxin level. The data also shows that the NTCD strain cannot be quantified by this method due to absence of toxin production. The growth rate data in **Figure 4.5b** follows a similar trend, with the untreated samples showing a steady exponential rise over time, whereas the vancomycin treated HTCD sample shows only a mild rise to 1.51 and 1.61 times after 4 and 24 hours, respectively, and the vancomycin treated NTCD sample shows only a minimal rise to 1.1 and 1.05 times, after 4 and 24 hours, respectively. Next, the DEP velocity data after various treatment periods (4 and 24 hours) is

compared to the toxin production level for the HTCD strain (**Figure 4.5c**), the growth rate data for the HTCD strain (**Figure 4.5d**) and the growth rate data for the NTCD strain (**Figure 4.5e**) over the same treatment periods (4 and 24 hours), with the respective value for the untreated sample at the same time period serving as the “control” (Un-0, Un-4 or Un-24). As per the toxin production levels in **Figure 4.5c**, while alterations to the HTCD strain are apparent after 24 hours of vancomycin treatment; i.e. a difference of 7.5 versus the control (Un-24) as per red solid lines along the X-direction, the alteration is just barely apparent after 4 hours of vancomycin treatment; i.e. a difference of just 0.55 versus the control (Un-4) as per green solid lines along the X-direction). On the other hand, the DEP data shows a significant reduction in velocity, from 30.7 $\mu\text{m/s}$ to 7.6 $\mu\text{m/s}$ (green dashed lines in the Y-direction), right from the first time point of 4 hours of vancomycin treatment, with further reduction to 4 $\mu\text{m/s}$ after 24 hours of vancomycin treatment. Similarly, the growth rate reduction of the HTCD strain is clear only after 24 hours of vancomycin treatment in **Figure 4.5d**, with a difference of 2.2 versus the control (Un-24), as per red solid lines in the X-direction. In comparison to the minimal growth rate reduction in the HTCD strain after 4 hours of vancomycin treatment, the respective reduction in the DEP velocity is substantial for the same 4 hour treatment time. For the NTCD strain, while the reduction in growth rate is apparent in **Figure 4.5e** after 24 hours of vancomycin treatment; i.e. a difference of 3.3 versus the untreated sample (Un-24) as per red solid lines in the X-direction, the alteration is not easily distinguishable after 4 hours of vancomycin treatment; i.e. a difference of 0.74 versus the untreated sample (Un-4), as per green solid lines in the X-direction. On the other hand, just as with the HTCD strain, reduction in the DEP velocity is substantial (16 $\mu\text{m/s}$ to ~ 7 $\mu\text{m/s}$) right from the first time point of 4 hours of vancomycin treatment, as per green dash lines in the Y-direction. Hence, since the DEP measurement method eliminates the need for microbial culture, which is required within conventional diagnostic methods for enhancing their sensitivity towards viable versus non-viable *C.difficile*, the DEP velocity measurement

method enables the quantification of microbial alterations at smaller antibiotic doses. Furthermore, the uncertainties are lowered with the DEP method, since comparisons are required against only a single control (i.e. against the DEP velocity of the untreated sample) rather than against multiple control samples, as required with toxin immunoassay and growth rate methods (i.e. against the respective values for untreated *C. difficile* after microbial culture over time periods equivalent to each antibiotic treatment time point). As a result, we envision that DEP methods can be applied more easily towards optimizing antibiotic dosage and discerning the mechanism of their action.

Inter-strain separations from mixed *C.difficile* samples

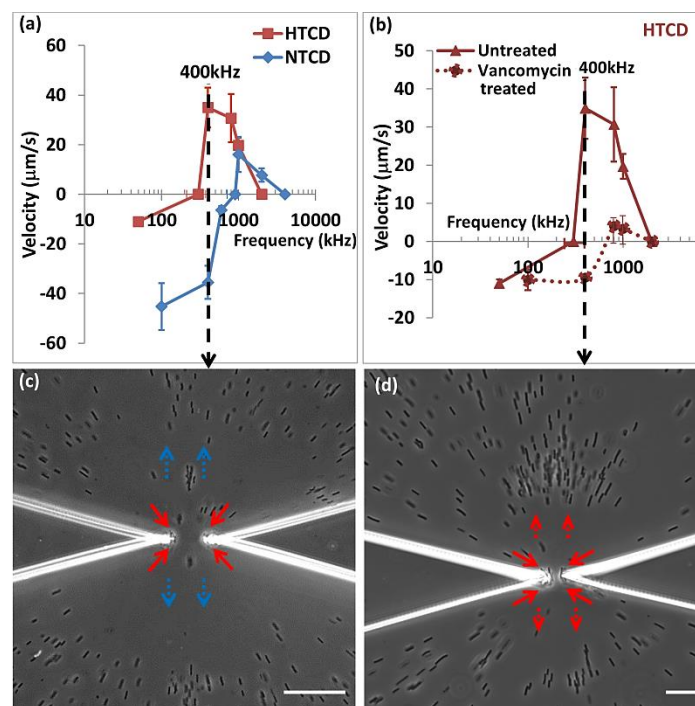


Figure 4.6 (a) Dielectrophoretic spectra of HTCD versus NTCD; (b) DEP spectra of HTCD after vancomycin treatment; (c) At 400 kHz, HTCD strain shows pDEP (red arrow) versus NTCD strain shows nDEP (blue arrow); (d) at 400 kHz, untreated HTCD strain shows pDEP (red solid arrow) versus vancomycin treated HTCD strain shows nDEP (red dotted arrow). Scale bar: 30 μm .

The quantitative DEP response measurements in **Figure 4.3b** and **Figure 4.4** suggest that particular *C.difficile* strains may be separated from each other based on their characteristic

electrophysiology, by identifying an appropriate frequency with maximum differences in the magnitude and direction of the DEP force. We choose the approach of accomplishing separations based on differences in direction of DEP force, since it can demonstrate the differential spatial localization of each strain-type within a few seconds. The heterogeneous samples we choose are: (i) a minority HTCD subpopulation within a majority population of NTCD strains with two-fold higher concentration; and (ii) a HTCD sample after incomplete antibiotic treatment over just 20 minutes, including a subpopulation of viable HTCD along with de-activated HTCD. For (i), as per **Figure 4.6a**, we choose a frequency of 400 kHz, wherein the HTCD strain exhibits strong pDEP behavior, while the NTCD strain continues to exhibit substantial nDEP. It is apparent from **Figure 4.6c**, that such a separation can be accomplished in a facile manner, as confirmed by the DEP response and toxin levels measured from pDEP trapped *C.difficile*. Similarly, using a 400 kHz field as indicated in Figure 5b for the separation of sample (ii), HTCD samples after vancomycin treatment at early time periods (20 minutes) show the presence of a *C.difficile* subpopulation with some viability (red solid arrows), along with a deactivated majority population (red dotted arrows) (**Figure 4.6d**), compared to vancomycin treated HTCD samples after 4 hours, thereby presenting a methodology to quantify the effectiveness of antibiotic treatments based on the DEP collection rate.

II. Single cell level analysis of the inhibitory effect of non-toxigenic *C.difficile* on toxigenic *C.difficile*

Introduction and Rational

C.difficile infection (CDI) is a toxin-mediated intestinal disease, which is commonly attributed to occur due to elimination of healthy microflora in the gut under administration of

broad-spectra antibiotics, followed by exposure to pathogenic *C.difficile* strains within a health-care facility¹⁴. CDI rates have exhibited a steady rise worldwide over the last two decades, with high morbidity and mortality. Metronidazole and vancomycin are the most commonly used antibiotics for CDI treatments. However, a number of studies have demonstrated the increasing treatment failure of patients experiencing disease recurrence with the same strain after the standard antibiotic treatments⁸¹.

Probiotic microorganisms are receiving increasing levels of interest towards development of prevention and treatment strategies for CDI⁸². To understand the inhibitory effect of probiotics on toxigenic *C.difficile* strains several methods ranging from cytotoxicity studies on animal models to in vitro functionality studies on *C.difficile* (growth, toxin production and colonization) have been utilized. For example, it has been shown that some lactic acid bacteria and yeasts can significantly protect hamster or mice from diarrhea, enterocolitis, as well as lower tissue damage and toxin levels triggered by *C. difficile*^{83, 84}. Furthermore, a number of studies have shown that the *Bifidobacterium* and *Lactobacillus* supernatants or in co-culture with *C. difficile* can inhibit *C.difficile* growth, cytotoxicity and adhesion ability to human enterocyte cell lines^{70, 85-87}.

Limitations of current methods

However, the results from the animal model and from the functionality of *C.difficile* only provide indirect mechanisms of the inhibitory effect on *C.difficile*. No prior studies have explored the inhibitory mechanisms directly on the *C.difficile* at a single cell level. Single cell analyses can provide invaluable insights into studying the inhibition effect of probiotic directly on *C.difficile*. For example, it has been shown that S(Surface)-layer glyco-proteins, which form a part of the cell wall envelope within both gram positive and gram negative bacteria, are integral towards surface recognition, colonization, host-pathogen adhesion and virulence⁸⁸. Using animal model to determine the colonization rates or using the enterocyte

cells lines adhesion assay to numerate the adhesion rates of *C.difficile* cannot provide the information on alterations in cell phenotype due to S-layers on the cell wall. Direct monitoring the alterations on single cells level can be used to directly correlate the influence of probiotics on cell phenotype, thereby providing strategies towards optimizing microflora for protection against CDI. Hence, there is a need for method to enable the simultaneous monitoring and quantifying the levels of physiological alterations of *C.difficile* at single-cells level.

Objectives

Not all strains of *C. difficile* produce toxins. Non-toxicogenic *C difficile* (NTCD) strains do not produce toxin A or toxin B due to the lack of Pathogenicity Locus (PaLoc), and are not typically implicated in symptomatic infection. In addition to the inhibitory effects of other probiotic micro-organisms against CDI, prior studies have shown that gastrointestinal colonization of patients and hamsters by the NTCD strains can reduce the incidence of CDI from TCD strains⁸⁹. Recent clinical trail 1 and 2 demonstrated the safety and efficacy of NTCD in healthy subjects and CDI patients^{65, 90}. Administration of NTCD as a “probiotic” would be a major milestone in the treatment of primary and recurrent CDI and would be an easier and more palatable option compared to fecal bacteriotherapy. However, the mechanism by which NTCD provides protection against CDI remains unclear. Herein, we seek to investigate the inhibitory effect of colonization ability of TCD by NTCD in single cells resolution.

Dielectrophoresis (DEP) causes the frequency-selective translation of polarized bio-particles under a spatially non-uniform electric field, either towards (by positive DEP or pDEP) or away (by negative DEP or nDEP) from the high field regions of a microfluidic device, depending on the polarizability of the bio-particle versus that of the medium. Hence, in spite of the heterogeneous nature of microbial samples, the frequency response of the DEP velocity

of individual cells towards or away from localized regions of a microfluidic device can be used to quantify the alterations in electrophysiology of each cell type. In our prior work, we have applied these capabilities towards the label-free distinction of intact *C. difficile* strains with systematic differences in cell wall morphology that occur due to their constituting S-layer, as correlated by an adhesion assay. We demonstrated that differences in cell wall roughness cause systematic differences in their DEP crossover frequency due to alterations in the net wall capacitance². In this current study, we seek to apply these DEP capabilities towards characterizing the electrophysiological alterations on TCD strains due to the antimicrobial and anti-adhesive effects of the thermolabile extracellular factors secreted by NTCD during co-culture, and correlate these phenotypic changes to the alterations in growth rate, toxin production and colonization of high toxigenic *C.difficile* (HTCD).

Results and Discussions

Inhibition of HTCD cell functionalities in NTCD supernatant and co-cultured with NTCD

We begin with examination of the functionality of HTCD cultured with an NTCD supernatant or co-cultured with NTCD. First, we measure the growth rates after the overnight culture of HTCD in various supernatants, including: fresh BHI broth, as positive control; cell-free HTCD supernatant (HTCD-S), as control and cell-free NTCD supernatant (**Figure 4.7a**). We normalize each growth rate to the growth rate of the cells cultured in BHI broth. For HTCD cultured in HTCD-S and NTCD-S, the growth rates reduce to about 60% of that obtained within BHI broth. We attribute this 40% growth reduction to the lack of nutrients for cell growth. Furthermore, since we do not see significant growth rate differences between HTCD cultured in HTCD-S versus NTCD-S, this suggests that the leftover nutrient levels in the HTCD-S and NTCD-S are quite similar. Next, we examine the growth rate of the HTCD

co-cultured with NTCD, but separated by a 0.4 μm pore size membrane, with the HTCD inoculate on either side of the membrane serving as the co-culture control. While the NTCD-S does not inhibit the growth of the HTCD, the HTCD co-culture with NTCD reduces the HTCD growth rate to only 80% of the co-culture control (**Figure 4.7a**). The toxin production level of HTCD-S and NTCD-S are about 80% and 70%, respectively, of their respective value of the HTCD control cultured in BHI (**Figure 4.7b**). However, for the case of HTCD co-cultured with NTCD, the HTCD toxin production level is inhibited to only 60% of the respective control for the co-culture. It is noteworthy that although the cell numbers are reduced by only 20% (**Figure 4.7a**), the toxin production is reduced by 40% (**Figure 4.7b**), compared to the co-culture control. This suggests that the toxin reduction is due to the inhibitory effect, rather than due to the lower cell numbers than the control.

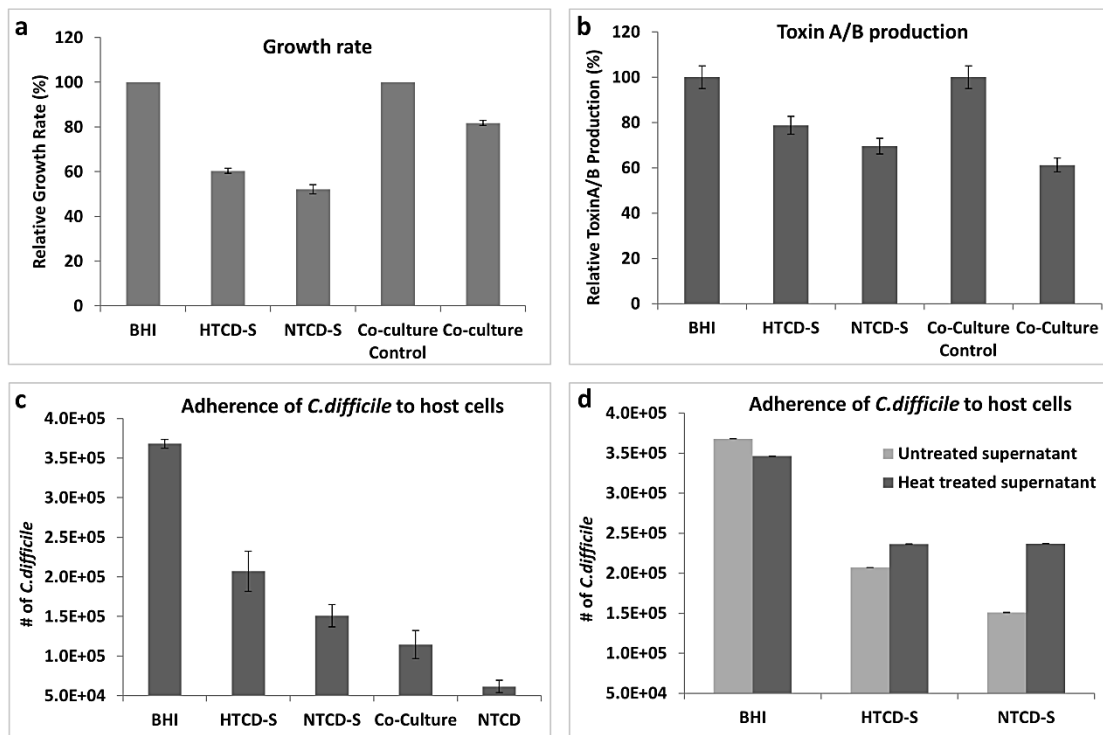


Figure 4.7 (a) Relative growth rate and (b) relative toxin production. Both growth rate and toxin production of the HTCD-S and NTCD-S are normalized to the BHI control (as 100%); and the co-culture is normalized to co-culture control (as 100%). Co-culture control is the HTCD inoculated on both side of the transwell. (c) Variations in adherence of each growth conditions to human colon epithelial cells by enumerating colony-forming units (CFU). (d) Variations in adherence of heat-treated supernatant versus untreated supernatant by enumerating colony-forming units (CFU).

Last, we examine the adhesion ability of the HTCD cells cultured in various supernatants versus HTCD cells co-cultured with NTCD. We measure the adhesion ability by numerating the HTCD adhered to the host cells on a colony forming unit assay. Note that the initial cell numbers are adjusted to equal before introducing the HTCD to the host cells for the adhesion assay. The HTCD cultured in BHI shows the strongest levels of adhesion to host cells, followed by HTCD cultured in HTCD-S, NTCD-S and finally HTCD co-cultured with NTCD, which shows an adhesion level just slightly higher than that of NTCD (**Figure 4.7c**). This confirms that upon the co-culture of HTCD with NTCD, the adhesion to host cells is significantly inhibited, compared to the BHI control. We attribute the lower host cell adhesion properties of HTCD in HTCD-S to the lack of nutrient (**Figure 4.7a**). It is noteworthy that while NTCD-S has a similar level of nutrients to the HTCD-S, as inferred based on their similar growth rate (**Figure 4.7a**), the larger reduction of cell adherence for HTCD cultured in NTCD-S versus that cultured in HTCD-S is likely due to extracellular factors in the NTCD-S, which inhibit the adherence of HTCD to the host cells. To examine the inhibition mechanism, we heat treated the supernatants to denature any heat sensitive factors. As per Fig. 1c, HTCD culture within this heat-treated NTCD-S significantly increases its adherence to host cells in comparison with HTCD cultured within untreated supernatants (**Figure 4.7c**). In fact, the net adhesion of HTCD cultured within heat-treated NTCD-S is similar to HTCD cultured in untreated HTCD-S, thereby suggesting that the lower adherence of HTCD in untreated NTCD-S can be attributed to the thermolabile extracellular factors in the NTCD-S.

Dielectrophoretic monitoring of HTCD modification

In our prior study, we have demonstrated that the morphological differences in the cell wall region of *C.difficile* strains, presumably due to differing S-layer glyco-protein levels as validated by their differing adhesion to a host cell, cause systematic variations in their crossover frequency (f_{xo}) for transition from negative to positive dielectrophoresis (DEP)

behavior due to their differing cell wall capacitances. We have shown that HTCD, with its improved ability for colonizing host cells exhibits a high level of net cell wall capacitance (low f_{xo}), followed by the LTCD (low-toxigenic *C.difficile*) and then by the NTCD strains. Based on the lower adherence to host cells, for HTCD cultured in NTCD-S versus HTCD cultured in HTCD-S (**Figure 4.7c**), we anticipate a shift in its DEP spectra towards higher frequencies, as quantified by the inflection point towards pDEP. In order to enhance the sensitivity of these differences towards the lower conductivity of cell wall properties versus that of the cytoplasm, we use a lower media conductivity (σ_m) of 0.05 S/m than was used to distinguish strains based on cell wall and cytoplasm properties (σ_m of 0.1 S/m was used in this latter case).

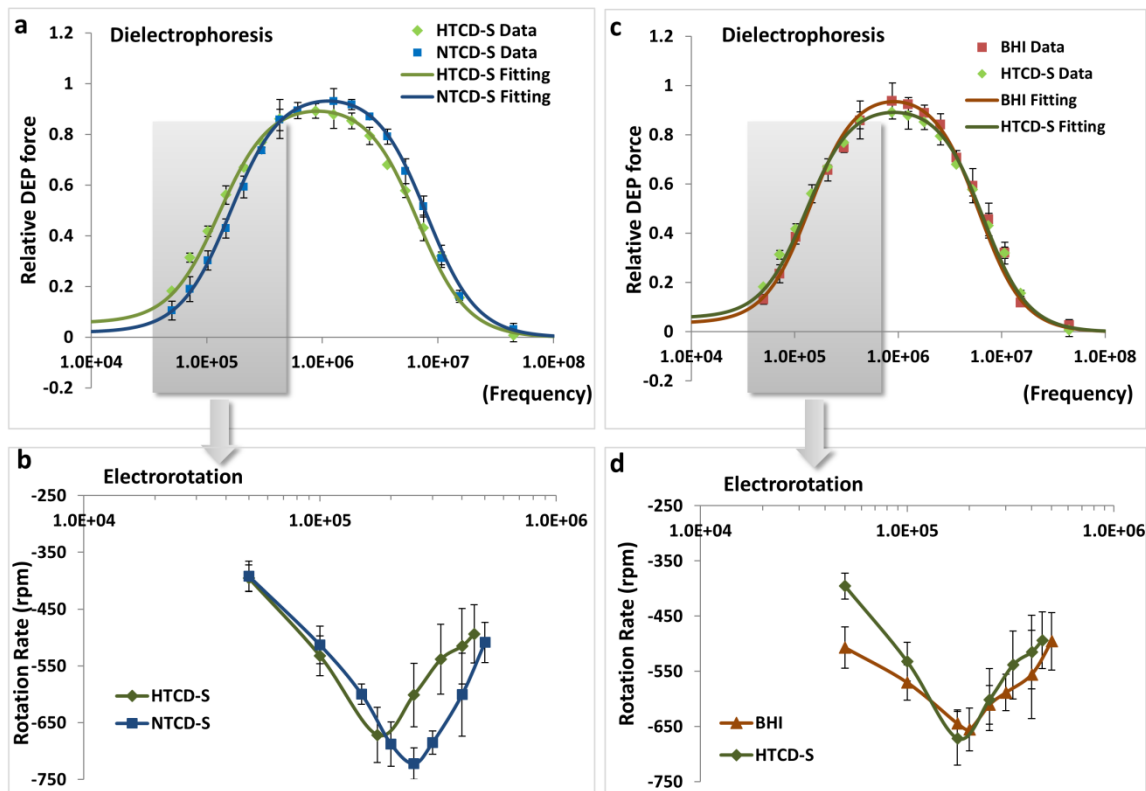


Figure 4.8 DEP frequency spectra (50kHz-45MHz) of HTCD-S versus NTCD-S (a), and BHI versus HTCD-S (c); and electrorotational frequency spectra (50kHz-500kHz) for HTCD-S vs NTCD-S (b) and BHI vs HTCD-S (d). (The data fitting is done by my group mate, Ali Rohani.)

As expected, the DEP spectra of HTCD cultured in NTCD-S is shifted towards higher

frequencies (**Figure 4.8a**), presumably due to a lower cell wall capacitance as shown in. The cell wall permittivity (ϵ) is seen to decrease from 10 S/m for HTCD cultured in HTCD-S, to 8 for HTCD cultured in NTCD-s. To confirm an up-shifting of the frequency, we utilized electrorotation to track the shift in peak of the counter-field rotation that corresponds to this shift in inflection of the DEP spectra. As shown in **Figure 4.8b**, the highest rotation rate for HTCD cultured in HTCD-S occurs at 175kHz, whereas the highest rotation rate for HTCD cultured in NTCD-S occurs at 250kHz. To confirm that the HTCD cells cultured in HTCD-S are unaltered in electrophysiology versus those cultured in BHI, we compare their DEP spectra. The DEP data shown in **Figure 4.8c** as well as the rotational data in **Figure 4.8d** provide this confirmation, with similar frequencies for the highest counter-field rotation rate (200kHz for HTCD cultured in BHI vs. 175 kHz for HTCD cultured in HTCD-s. This in turn enhances the confidence levels for the differences in DEP response of HTCD cultured in NTCD-S versus HTCD cultured in HTCD-S. Hence, while the reduction in growth rate, toxin production and host cell adhesion for HTCD cultured in HTCD-S can be related to the lack of nutrients, these fewer nutrients do not significantly change the electrophysiological characteristics of the HTCD cells, whereas for HTCD cultured in NTCD-S, the electrophysiology is significantly altered.

Finally, based on the highest host cell adherence characteristics of HTCD cultured in BHI, follow by lower respective levels for HTCD co-cultured with NTCD, and even lower levels for NTCD cells (**Figure 4.7c**), we anticipate a shift in the DEP spectra of HTCD co-cultured with NTCD towards a higher inflection point than for HTCD co-cultured control. As expected, the co-culture shows significant shifting of the frequency to higher values due to the decreasing cell wall capacitance as shown in **Figure 4.9a**, and the shift of DEP spectra is closer to that of the NTCD. The membrane permittivity of control, co-culture and NTCD are: 10 S/m, 6 S/m and 4 S/m, respectively. The co-culture also shows higher antibiotic susceptibility compared to the co-culture control (**Figure 4.9b**).

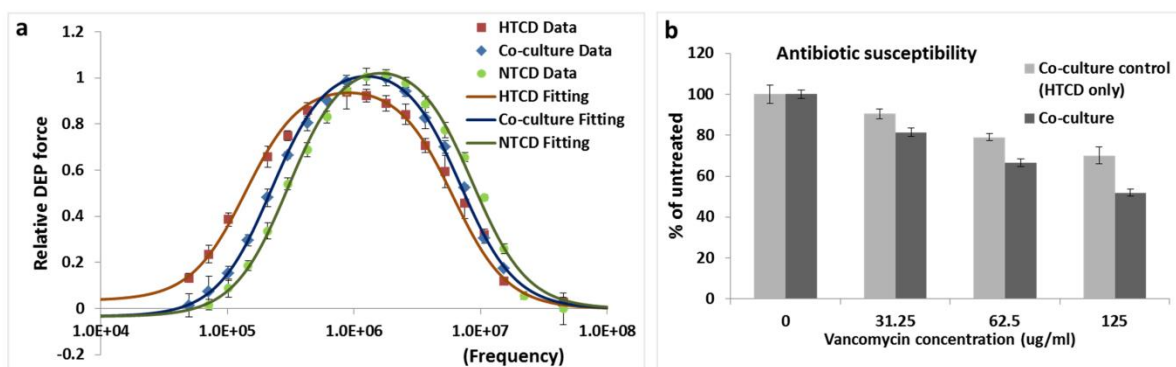


Figure 4.9 (a) DEP frequency spectra (50kHz-45MHz) of Co-culture control, co-culture and NTCD. (b) Antibiotic susceptibility of co-culture control versus co-culture. The vancomycin treated groups are normalized to the untreated (0 vancomycin, as 100%). (The data fitting is done by my group mate, Ali Rohani.)

III. Conclusions

In the first section, we demonstrate that morphological differences in the cell wall region of *C.difficile* strains, presumably due to differing S-layer glyco-protein levels as validated by their differing adhesion to a host cell, cause systematic variations in their crossover frequency for transition from negative to positive dielectrophoresis (DEP) behavior. As a result, the DEP spectra exhibit characteristic features that may be applied towards independently monitoring each *C.difficile* strain with differing S-layers, as well as towards inter-strain separation of intact cells from mixed *C.difficile* samples. Through benchmarking the DEP data against conventional measures of *C.difficile* activity, such as toxin production and growth rate, we demonstrate its superior sensitivity towards characterizing microbial alterations upon vancomycin treatment, thereby enabling the application of DEP methods towards the optimization of antibiotic treatments. Finally, through appropriate choice of frequency of the applied field, we demonstrate proof-of-concept separation of subpopulations of high-toxigenic *C.difficile* strains from a sample of non-toxigenic *C.difficile*, based on the direction of their dielectrophoresis behavior. In this manner, we present a methodology for

isolation of individual strains from mixed *C.difficile* samples, quantification of antibiotic treatments and the engineering of nutrient environments to control microbiomes.

In the second section, we demonstrated the ability of frequency-resolved DEP to selectively probe particular intracellular regions, such as the S-layer on the cell wall at low frequencies (< 250 kHz) and the cytoplasm electrophysiology at high frequencies (1 MHz) versus current methods based on overall microbial viability. Specifically, we show that the inflection in the DEP spectra that is related to alterations in cell wall capacitance can be utilized to predict the colonization ability of *C.difficile* cells within just a few minutes, which is consistent with the *C.difficile* adhesion assay on host cells (HCT8) that takes ~24 hours. Utilizing this tool, we show that HTCD cells co-cultured with NTCD exhibit a significantly lowered cell wall capacitance and adherence properties to host cells versus HTCD cells cultured in cell-free NTCD supernatant. We show that this reduction in colonization ability of HTCD, presumably due to the alterations of their S-layers during co-culture with NTCD strains, can be attributed to the release of thermo-labile growth factors during the co-culture, which is not the case for HTCD cells cultured in cell-free HTCD supernatant or for HTCD cells cultured in the standard BHI media. Additionally, we also showed that HTCD cells become more susceptible to antibiotic treatment after co-culture with NTCD cells.

Chapter 5

Conclusion and Future work

Conclusion

In this dissertation, we have demonstrated the application of a microfluidic device based on DEP towards the separation and discrimination of different micro-organisms, based on their inherent electrophysiology. In contrast to the current state of art utilizing DC fields within an electrode-less device geometry, we have applied AC fields to monitor intact microbials based on their cell wall characteristics at low frequencies and on their cytoplasmic alterations at higher frequencies. As a result, we demonstrate the ability to identify particular frequencies for distinguishing and separating microbials based on subtle differences in their intracellular electrophysiology, which is especially significant in microbiological organisms. We have applied these single particle DEP tracking methods towards characterization and separation of persistent microbial sub-populations and those from different microbial strains; as well as for studying the alterations to microbial cells due to inter-microbial interactions across the host microbiome.

In Chapter three, we show that DEP technique is capable of separating and characterizing the subpopulations of *Cryptosporidium parvum* oocysts after heat and AgNP treatments. We utilize insulator constrictions in a microfluidic channel to spatially modulate the localized field over the extent needed for defining oocyst trajectories and for obtaining high-resolution displacement versus time measurements under both, positive and negative dielectrophoresis. As a result, we are able to simultaneously track multiple oocysts in parallel, with single particle sensitivity. In this manner, DEP tracking and measurement method is more sensitive to differences in electrophysiology from fractional sub-populations. Through correlating the force response in the 0.4–1 MHz range to integrity

of sporozoites in the oocyst and at ≤ 100 kHz to the integrity of the oocyst wall, DEP can characterize disinfection mechanism of oocysts upon heat treatment and AgNP treatment, based on differences of their membrane and cytoplasm electrophysiology versus untreated oocysts. We also apply DEP to demonstrate the disinfection action with different AgNP capping-layers, for potential optimization in water treatment methods.

In Chapter four, we show that DEP technique can independently monitor and separate particular *C.difficile* strains (high-toxigenic, low toxigenic and non-toxigenic *C.difficile* strains) due to alterations in their S-layers, which cause characteristic alterations in their electrophysiology. Furthermore, through benchmarking the DEP data against conventional measures of *C. difficile* functionality, such as toxin production and growth rate, we demonstrate its superior sensitivity toward characterizing microbial alterations upon vancomycin treatment, thereby enabling the application of DEP methods toward the optimization of antibiotic treatments. We also demonstrate these capabilities of DEP towards characterization of the electrophysiological alterations on toxigenic *C.difficile* (TCD) strains due to the antimicrobial and anti-adhesive effects of the thermolabile extracellular factors secreted by non-toxigenic *C.difficile*, as a probiotic during co-culture, and correlate these phenotypic changes to the alterations in growth rate, toxin production and colonization of TCD. The effects are more prominent when the HTCD are co-cultured with NTCD than the HTCD are cultured in cell-free NTCD supernatant.

Based on the results, we envision the highly sensitive, label-free and non-destructive features of DEP analysis, which enable the characterization of heterogeneous subpopulations and the monitoring of antibiotic-induced alterations at earlier times, thereby aiding in the development of antibiotic treatments with lower dosages. Furthermore, we envision the application of DEP techniques towards studying the interaction of other probiotics with TCD strains in a dynamic co-culture with single-cells level resolution, for characterizing the

electrophysiological alterations in a non-destructive and label-free manner for optimizing the microflora.

Future work

While we demonstrated some applications of utilizing DEP for characterization and separation of micro-organisms, there are still many related work to be explored. In the following, we suggest some potential future work for further investigation:

DEP separation of *C.difficile* from other microbials in fecal samples

DEP force is highly dependent on particle size, shape of the particle and the dielectric contrast of polarizability between the particle and the medium, as mentioned in Chapter 2. Given the nature of high aspect ratio rod-shape and high cytoplasmic conductivity of *C.difficile*, we show below the capability for DEP separation of *C.difficile* from other microbials. In **Figure 5.1**, we demonstrate the strong pDEP behavior of *C.difficile* at 400 kHz can be utilized to separate it from *E.coli*, which exhibits nDEP at this frequency due to its smaller size ($\sim 1\mu\text{m}$) and lower cytoplasm conductivity. In **Figure 5.2a**, we also show the strong pDEP behavior of *C.difficile* at 400 kHz can be utilized to separate it from yeast, which exhibits nDEP behavior at this frequency due to its spherical shape and lower cytoplasm conductivity.

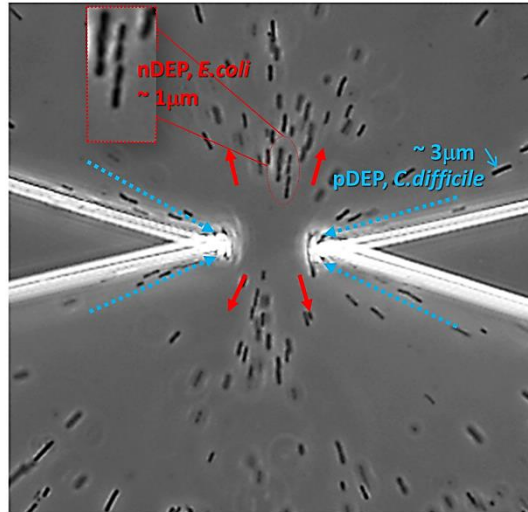


Figure 5.1 The *C.difficile* strain shows strong pDEP at 400 kHz, whereas *E.coli* shows nDEP.

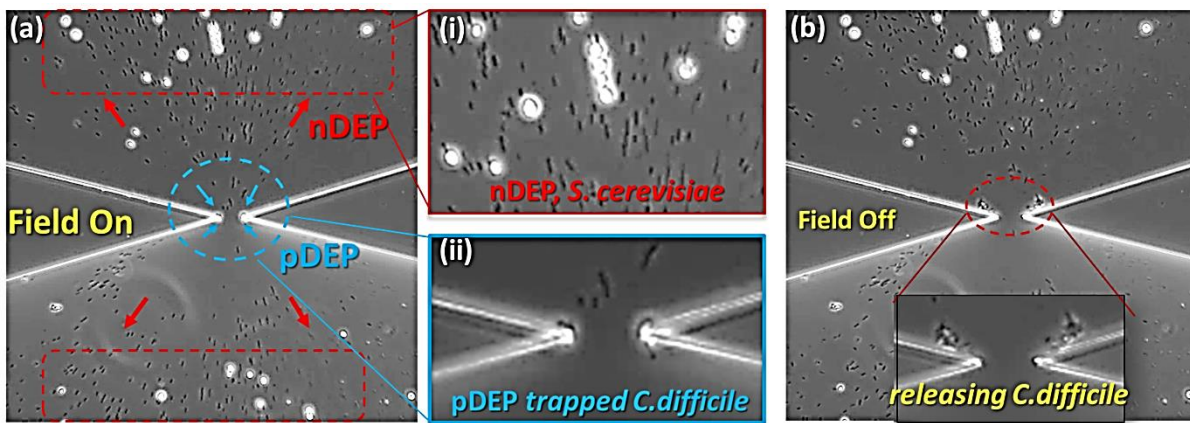


Figure 5.2 The *C.difficile* shows strong pDEP at 400 kHz, whereas yeast shows nDEP when the field is on (a) and off (b) where the *C.difficile* were released from the tips of the constrictions.

Current methods for *C.difficile* infection (CDI) detection relies on stool culture, PCR and cytotoxicity assay. However, these methods can take hours to days for diagnostic. In these preliminary results, we demonstrate that DEP can separate gram positive (*C.difficile*) versus gram negative (*E.coli*) bacteria, and prokaryote (*C.difficile*) and eukaryote (yeast). Hence, we propose DEP can be a potential tool to separate *C.difficile* from complex fecal samples.

DEP separation of *C.difficile* from probiotics after mixed culture

In Chapter four, we show the antimicrobial and anti-adhesive effects of the thermolabile extracellular factors secreted by NTCD during co-culture with HTCD. Studies also shown

supernatants from other probiotics or in co-culture with *C. difficile* can inhibit *C. difficile* growth, cytotoxicity and adhesion ability to human enterocyte cell lines^{70, 85}. However, besides the inhibition effect of the secreted factors in the supernatants, it has been shown that the inhibition of cytotoxicity effect only occurs when placed in mixed cultured with *C. difficile*, whereas when it is co-cultured with *C. difficile* separated by a permeable membrane or using its cell-free supernatant, it has no inhibition effect on *C. difficile*⁸⁷. In addition, S-layer proteins from *Lactobacillus kefir* have been shown to antagonize cytotoxicity effect on *C. difficile*⁹¹. This suggests the inhibition effect of probiotics also rely on direct cell-cell interaction between strains. The emerging interest in restoration of a healthy microbiota with fecal transplantation or probiotics to treat CDI further highlights the need to understand the complex and dynamic interaction between the commensal polymicrobial environment and TCD. However, there are no suitable methods to separate the *C. difficile* from mixed culture for further cell functionality and cell physiology analysis. Based on the results in Chapter 4 and the preliminary results in **Figure 5.1** and **5.2**, we propose to first separate TCD from other mixed cultured microbials based on differences in DEP at critical frequencies¹⁸, and correlate the alterations in the S-layer on the *C. difficile* cell wall based on their electrophysiology to its colonization ability to host cells.

Bibliography

1. Y. H. Su, M. Tsegaye, W. Varhue, K. T. Liao, L. S. Abebe, J. A. Smith, R. L. Guerrant and N. S. Swami, *The Analyst*, 2014, **139**, 66-73.
2. Y. H. Su, C. A. Warren, R. L. Guerrant and N. S. Swami, *Analytical chemistry*, 2014, **86**, 10855-10863.
3. W. H. Organization, *World Health Organization Report*, 2014.
4. K. R. Allison, M. P. Brynildsen and J. J. Collins, *Current opinion in microbiology*, 2011, **14**, 593-598.
5. A. M. Foudeh, T. Fatanat Didar, T. Veres and M. Tabrizian, *Lab on a chip*, 2012, **12**, 3249-3266.
6. E. K. Sackmann, A. L. Fulton and D. J. Beebe, *Nature*, 2014, **507**, 181-189.
7. N. G. G. Hywel Morgan, in *AC Electrokinetics: Colloids and Nanoparticles*, USA: Research Studies Press Ltd., First edn., 2002, p. 250.
8. R. Pethig, *Biomechanics*, 2010, **4**.
9. A. Rohani, W. Varhue, Y. H. Su and N. S. Swami, *Electrophoresis*, 2014, **35**, 1795-1802.
10. T. B. Jones, *Electromechanics of particles*, Cambridge University Press, Cambridge ; New York, 1995.
11. F. Davis, M. A. Hughes, A. R. Cossins and S. P. J. Higson, *Anal Chem*, 2007, **79**, 1153-1157.
12. C. M. Carey, H. Lee and J. T. Trevors, *Water research*, 2004, **38**, 818-862.
13. H. V. Smith, R. A. Nichols and A. M. Grimason, *Trends in parasitology*, 2005, **21**, 133-142.
14. M. Rupnik, M. H. Wilcox and D. N. Gerding, *Nature reviews. Microbiology*, 2009, **7**, 526-536.
15. S. M. Poutanen and A. E. Simor, *CMAJ : Canadian Medical Association journal = journal de l'Association medicale canadienne*, 2004, **171**, 51-58.
16. C. Ghose, *Emerging Microbes and Infections*, 2013, **2**.
17. V. Chaurey, A. Rohani, Y. H. Su, K. T. Liao, C. F. Chou and N. S. Swami, *Electrophoresis*, 2013, **34**, 1097-1104.
18. V. Farmehini, A. Rohani, Y. H. Su and N. S. Swami, *Lab on a chip*, 2014, **14**, 4183-4187.
19. K. F. Hoettges, Y. Hubner, L. M. Broche, S. L. Ogin, G. E. Kass and M. P. Hughes, *Analytical chemistry*, 2008, **80**, 2063-2068.
20. F. H. Labeed, J. Lu, H. J. Mulhall, S. A. Marchenko, K. F. Hoettges, L. C. Estrada, A. P. Lee, M. P. Hughes and L. A. Flanagan, *PloS one*, 2011, **6**, e25458.
21. H. J. Mulhall, F. H. Labeed, B. Kazmi, D. E. Costea, M. P. Hughes and M. P. Lewis,

- Analytical and bioanalytical chemistry*, 2011, **401**, 2455-2463.
22. A. Rohani, W. Varhue, Y. H. Su and N. S. Swami, *Biomicrofluidics*, 2014, **8**, 052009.
 23. O. Gefen and N. Q. Balaban, *FEMS microbiology reviews*, 2009, **33**, 704-717.
 24. E. J. Stewart, *Journal of bacteriology*, 2012, **194**, 4151-4160.
 25. K. K. C. T. Mark Smith, *Cryptosporidium: The Analytical Challenge*, Cambridge: Royal Society of Chemistry, 2001.
 26. U. N. H. S. Programme, *Water and Sanitation in the World's Cities: Local Action for Global Goals*, Earthscan Publications, London, 2003.
 27. X. M. Chen, J. S. Keithly, C. V. Paya and N. F. LaRusso, *The New England journal of medicine*, 2002, **346**, 1723-1731.
 28. R. Dillingham and R. L. Guerrant, *Lancet*, 2004, **363**, 94-95.
 29. C. G. R. Kenneth J. Ryan, *Sherris Medical microbiology: An introduction to infectious disease*, New York: McGraw-Hill, Fourth edn., 2004.
 30. H. V. Smith and R. A. Nichols, *Experimental parasitology*, 2010, **124**, 61-79.
 31. P. C. Okhuysen, C. L. Chappell, J. H. Crabb, C. R. Sterling and H. L. DuPont, *J Infect Dis*, 1999, **180**, 1275-1281.
 32. M. Walker, K. Leddy and E. Hager, *Applied and environmental microbiology*, 2001, **67**, 5526-5529.
 33. J. B. Parr, J. E. Sevilleja, A. Samie, C. Alcantara, S. E. Stroup, A. Kohli, R. Fayer, A. A. Lima, E. R. Houpt and R. L. Guerrant, *The American journal of tropical medicine and hygiene*, 2007, **76**, 938-942.
 34. J. T. Connelly, S. R. Nugen, W. Borejsza-Wysocki, R. A. Durst, R. A. Montagna and A. J. Baumner, *Analytical and bioanalytical chemistry*, 2008, **391**, 487-495.
 35. Z. R. Gagnon, *Electrophoresis*, 2011, **32**, 2466-2487.
 36. D. J. Bakewell and H. Morgan, *Meas Sci Technol*, 2004, **15**, 254-266.
 37. F. H. Labeed, H. M. Coley and M. P. Hughes, *Bba-Gen Subjects*, 2006, **1760**, 922-929.
 38. Z. Gagnon, J. Gordon, S. Sengupta and H. C. Chang, *Electrophoresis*, 2008, **29**, 2272-2279.
 39. Z. Gagnon, J. Mazur and H. C. Chang, *Biomicrofluidics*, 2009, **3**.
 40. M. Castellarnau, A. Errachid, C. Madrid, A. Juarez and J. Samitier, *Biophysical journal*, 2006, **91**, 3937-3945.
 41. A. Di Biasio, L. Ambrosone and C. Cametti, *Biophysical journal*, 2010, **99**, 163-174.
 42. K. V. Kaler and T. B. Jones, *Biophysical journal*, 1990, **57**, 173-182.
 43. H. Watarai, T. Sakamoto and S. Tsukahara, *Langmuir*, 1997, **13**, 2417-2420.
 44. H. S. Moyed and K. P. Bertrand, *Journal of bacteriology*, 1983, **155**, 768-775.
 45. C. Marambio-Jones and E. M. V. Hoek, *J Nanopart Res*, 2010, **12**, 1531-1551.
 46. E. K. Fauss, R. I. MacCusprie, V. Oyanedel-Craver, J. A. Smith and N. S. Swami,

- Colloids and surfaces. B, Biointerfaces*, 2014, **113**, 77-84.
47. V. A. Oyanedel-Craver and J. A. Smith, *Environmental science & technology*, 2008, **42**, 927-933.
 48. B. De Gusseme, T. Hennebel, E. Christiaens, H. Saveyn, K. Verbeken, J. P. Fitts, N. Boon and W. Verstraete, *Water research*, 2011, **45**, 1856-1864.
 49. Y. H. Lv, H. Liu, Z. Wang, S. J. Liu, L. J. Hao, Y. H. Sang, D. Liu, J. Y. Wang and R. I. Boughton, *J Membrane Sci*, 2009, **331**, 50-56.
 50. J. R. Morones, J. L. Elechiguerra, A. Camacho, K. Holt, J. B. Kouri, J. T. Ramirez and M. J. Yacaman, *Nanotechnology*, 2005, **16**, 2346-2353.
 51. R. Fayer, *Applied and environmental microbiology*, 1994, **60**, 2732-2735.
 52. A. T. Campbell, L. J. Robertson and H. V. Smith, *Applied and environmental microbiology*, 1992, **58**, 3488-3493.
 53. H. Narayanan Unni, D. Hartono, L. Yue Lanry Yung, M. Mah-Lee Ng, H. Pueh Lee, B. Cheong Khoo and K. M. Lim, *Biomicrofluidics*, 2012, **6**, 12805-1280514.
 54. L. J. Anguish and W. C. Ghiorse, *Applied and environmental microbiology*, 1997, **63**, 724-733.
 55. H. Borowski, P. L. Clode and R. C. Thompson, *Trends in parasitology*, 2008, **24**, 509-516.
 56. Z. A. Kuznar and M. Elimelech, *Langmuir*, 2005, **21**, 710-716.
 57. W. A. Braff, D. Willner, P. Hugenholtz, K. Rabaey and C. R. Buie, *PloS one*, 2013, **8**, e76751.
 58. P. V. Jones, A. F. DeMichele, L. Kemp and M. A. Hayes, *Analytical and bioanalytical chemistry*, 2014, **406**, 183-192.
 59. B. H. Lapizco-Encinas, R. V. Davalos, B. A. Simmons, E. B. Cummings and Y. Fintschenko, *Journal of microbiological methods*, 2005, **62**, 317-326.
 60. K. C. Carroll and J. G. Bartlett, *Annu Rev Microbiol*, 2011, **65**, 501-521.
 61. M. Natarajan, S. T. Walk, V. B. Young and D. M. Aronoff, *Anaerobe*, 2013, **22**, 1-5.
 62. S. P. Sambol, M. M. Merrigan, J. K. Tang, S. Johnson and D. N. Gerding, *J Infect Dis*, 2002, **186**, 1781-1789.
 63. K. J. Nagaro, S. T. Phillips, A. K. Cheknis, S. P. Sambol, W. E. Zukowski, S. Johnson and D. N. Gerding, *Antimicrob Agents Ch*, 2013, **57**, 5266-5270.
 64. J. K. Shim, S. Johnson, M. H. Samore, D. Z. Bliss and D. N. Gerding, *Lancet*, 1998, **351**, 633-636.
 65. S. A. Villano, M. Seiberling, W. Tatarowicz, E. Monnot-Chase and D. N. Gerding, *Antimicrobial agents and chemotherapy*, 2012, **56**, 5224-5229.
 66. S. H. Cohen, D. N. Gerding, S. Johnson, C. P. Kelly, V. G. Loo, L. C. McDonald, J. Pepin, M. H. Wilcox, A. Society for Healthcare Epidemiology of and A. Infectious Diseases Society of, *Infection control and hospital epidemiology : the official journal of the*

- Society of Hospital Epidemiologists of America*, 2010, **31**, 431-455.
67. J. J. Hunt and J. D. Ballard, *Microbiology and molecular biology reviews : MMBR*, 2013, **77**, 567-581.
 68. P. Spigaglia and P. Mastrantonio, *Journal of clinical microbiology*, 2002, **40**, 3470-3475.
 69. B. G. Hawkins, C. Huang, S. Arasanipalai and B. J. Kirby, *Analytical chemistry*, 2011, **83**, 3507-3515.
 70. F. M. Trejo, J. Minnaard, P. F. Perez and G. L. De Antoni, *Anaerobe*, 2006, **12**, 186-193.
 71. M. M. Merrigan, A. Venugopal, J. L. Roxas, F. Anwar, M. J. Mallozzi, B. A. Roxas, D. N. Gerding, V. K. Viswanathan and G. Vedantam, *PloS one*, 2013, **8**, e78404.
 72. R. Govind and B. Dupuy, *PLoS pathogens*, 2012, **8**, e1002727.
 73. K. Mukherjee, S. Karlsson, L. G. Burman and T. Akerlund, *Microbiology*, 2002, **148**, 2245-2253.
 74. C. B. Reynolds, J. E. Emerson, L. de la Riva, R. P. Fagan and N. F. Fairweather, *PLoS pathogens*, 2011, **7**, e1002024.
 75. G. Sekot, G. Posch, P. Messner, M. Matejka, X. Rausch-Fan, O. Andrukhov and C. Schaffer, *Journal of dental research*, 2011, **90**, 109-114.
 76. E. Calabi, F. Calabi, A. D. Phillips and N. F. Fairweather, *Infect Immun*, 2002, **70**, 5770-5778.
 77. T. B. Jones, *Electromechanics of Particles*, Cambridge, New York: Cambridge University Press, 2005.
 78. H. M. a. N. G. Green, *AC Electrokinetics: Colloids and Nanoparticles*, 2003.
 79. P. R. Gascoyne, S. Shim, J. Noshari, F. F. Becker and K. Stemke-Hale, *Electrophoresis*, 2013, **34**, 1042-1050.
 80. M. Gerber, C. Walch, B. Loffler, K. Tischendorf, U. Reischl and G. Ackermann, *Journal of medical microbiology*, 2008, **57**, 776-783.
 81. G. C. Parkes, J. D. Sanderson and K. Whelan, *The Lancet infectious diseases*, 2009, **9**, 237-244.
 82. B. C. Johnston, S. S. Ma, J. Z. Goldenberg, K. Thorlund, P. O. Vandvik, M. Loeb and G. H. Guyatt, *Annals of internal medicine*, 2012, **157**, 878-888.
 83. F. M. Trejo, G. L. De Antoni and P. F. Perez, *The Journal of dairy research*, 2013, **80**, 263-269.
 84. P. A. Bolla, P. Carasi, L. Bolla Mde, G. L. De Antoni and L. Serradell Mde, *Anaerobe*, 2013, **21**, 28-33.
 85. P. Banerjee, G. J. Merkel and A. K. Bhunia, *Gut pathogens*, 2009, **1**, 8.
 86. F. M. Trejo, P. F. Perez and G. L. De Antoni, *Antonie van Leeuwenhoek*, 2010, **98**, 19-29.

87. T. D. Woo, K. Oka, M. Takahashi, F. Hojo, T. Osaki, T. Hanawa, S. Kurata, H. Yonezawa and S. Kamiya, *Journal of medical microbiology*, 2011, **60**, 1617-1625.
88. R. P. Fagan and N. F. Fairweather, *Nature reviews. Microbiology*, 2014, **12**, 211-222.
89. S. P. Sambol, M. M. Merrigan, J. K. Tang, S. Johnson and D. N. Gerding, *J Infect Dis*, 2002, **186**, 1781-1789.
90. D. N. Gerding, T. Meyer, C. Lee, S. H. Cohen, U. K. Murthy, A. Poirier, T. C. Van Schooneveld, D. S. Pardi, A. Ramos, M. A. Barron, H. Chen and S. Villano, *Jama*, 2015, **313**, 1719-1727.
91. P. Carasi, F. M. Trejo, P. F. Perez, G. L. De Antoni and L. Serradell Mde, *Anaerobe*, 2012, **18**, 135-142.